The Thesis Committee for Alexander Peter Joseph Lamb
Certifies that this is the approved version of the following thesis:

An Investigation of Anisotropy Using AVAZ and Rock Physics Modeling in the Woodford Shale, Anadarko Basin, OK

APPROVED BY
SUPERVISING COMMITTEE:

Supervisor:

Robert H. Tatham

Kyle T. Spikes

Mrinal K. Sen

An Investigation of Anisotropy Using AVAZ and Rock Physics Modeling in the Woodford Shale, Anadarko Basin, OK

by

Alexander Peter Joseph Lamb, B.S.; B.S.

Thesis

Presented to the Faculty of the Graduate School of

The University of Texas at Austin

in Partial Fulfillment

of the Requirements

for the Degree of

Master of Science in Geological Sciences

The University of Texas at Austin

May 2012

Dedication

I dedicate this thesis to my loving parents, Corey Patterson and Peter Lamb, and my best friend, Allison Lewis. Their support and passion for learning has inspired me to become the student and person I am today. Thank you for your love and guidance.

Acknowledgements

I would like to extend my deepest appreciation to my advisor, Dr. Robert Tatham. Without his support, my attendance and growth as a student at the University of Texas would not have been possible. Dr. Tatham's guidance and advice was invaluable to this project. I am also very grateful to Dr. Kyle Spikes, whose direction and help with rock physics modeling provided the framework to complete my work. Also, the support from Dr. Mrinal Sen was very appreciated throughout this project and our discussions gave me confidence to undertake the scope of this thesis.

Sincere thanks to Thomas Hess for his technical support and eagerness to help regardless of the situation. I also thank fellow graduate students Terence Campbell, Russell Carter, and Kyle Meyer whose discussions and personal support helped shape my experience at the University of Texas for the better.

Finally, I want to offer heartfelt gratitude to the Jackson School of Geosciences at the University of Texas, whose supportive environment fostered learning, discussion, and ongoing professional development.

Abstract

An Investigation of Anisotropy Using AVAZ and Rock Physics Modeling in the Woodford Shale, Anadarko Basin, OK

Alexander Peter Joseph Lamb, M.S. Geo. Sci.

The University of Texas at Austin, 2012

Supervisor: Robert H. Tatham

The Woodford Shale formation is currently an important unconventional gas resource that extends across parts of the mid-continent of the United States. A resource shale acts as source, seal, and reservoir, and its characterization is vital to successful exploitation and production of hydrocarbons.

This work is a surface seismic observation and investigation of the seismic anisotropy present in the Woodford Shale formation in the Anadarko Basin, Oklahoma. One of the main causes of anisotropy here is commonly believed to be vertical natural fractures (HTI) and horizontal alignment of clay minerals (VTI). Understanding the natural fracture orientation and density, as well as regional stress orientation, is important to the development of hydraulic fracturing programs in shales, such as the Woodford, producing natural gas. Dipole sonic log measurements in vertical boreholes suggest that the Woodford does possess vertical transverse isotropy (VTI), due possibly to horizontal layering or aligned clay minerals. Further, the borehole logs do not indicate horizontal transverse isotropy (HTI) associated with fracturing in the Woodford interval. An

amplitude varying with angle and azimuth (AVAZ) analysis was applied to 3-D surface seismic data in the Anadarko Basin and shows the dipole sonic logs may not be completely characterizing the anisotropy observed in the Woodford. Once this apparent contradiction was discovered, additional work to characterize the fractures in the formation was undertaken. A petrophysical model based on the borehole data of the Woodford Shale was created, combining various techniques to simulate the rock properties and behavior. With a more complete rock physics model, a full stiffness tensor for the rock was obtained. From this model, synthetic seismic data were generated to compare to the field data. Furthermore, analytic equations were developed to relate crack density to AVAZ response. Currently, the application of this AVAZ method shows fracture orientation and *relative* variations in fracture density over the survey area. This work shows a direction for a quantified fracture density because the synthetic seismic data has a quantified fracture density at its basis. This allowed for a relationship to be established between explicit fracture parameters (such as fracture density) and AVAZ results and subsequently may be used to create regional descriptions of fracture and/or stress orientation and density.

Table of Contents

List of Tables

List of Figures

Chapter I: Introduction

Background Of Shale Gas Production

Shale is commonly described as a fine-grained, clastic sedimentary rock composed of a mixture of clay minerals and silt-sized particles of other minerals, especially quartz and calcite. Shales that contain kerogen, however, can act as a potential source of hydrocarbon; these shales are often referred to as oil or gas shales. While the existence of large amounts of hydrocarbons in shales has been known for decades, shales, due to their low permeability, had often been viewed as effective sources or seals for accumulation in hydrocarbon reservoirs. Recent developments in horizontal drilling and hydraulic fracturing, however, have opened oil and gas shale reservoirs for exploitation and production. Following the 1991 development of the Barnett Shale in north Texas using horizontal wells, the expansion of the gas shale industry has rapidly increased. In North America alone, numerous shale reservoirs are currently producing at high volumes: for example, the Woodford, Antrim, Bakken, Bossier, Marcellus, and Eagle Ford formations (Figure 1.1). This advancement in gas production is primarily due to the refinement of both horizontal drilling and hydraulic fracturing, which stimulates fractures and increases permeability in the shale by injecting water, sand, and chemicals into the formation at high pressure, allowing gas flow from a previously tight source rock into the horizontal well.

While shale development has become more common, it still differs from the development of tight gas sandstones. Statistically, sandstones produce more volume initially, but shale wells are predicted to produce consistently for 30 years or more in some cases once production stabilizes (Frantz and Jochen, 2005). Shale reservoirs include

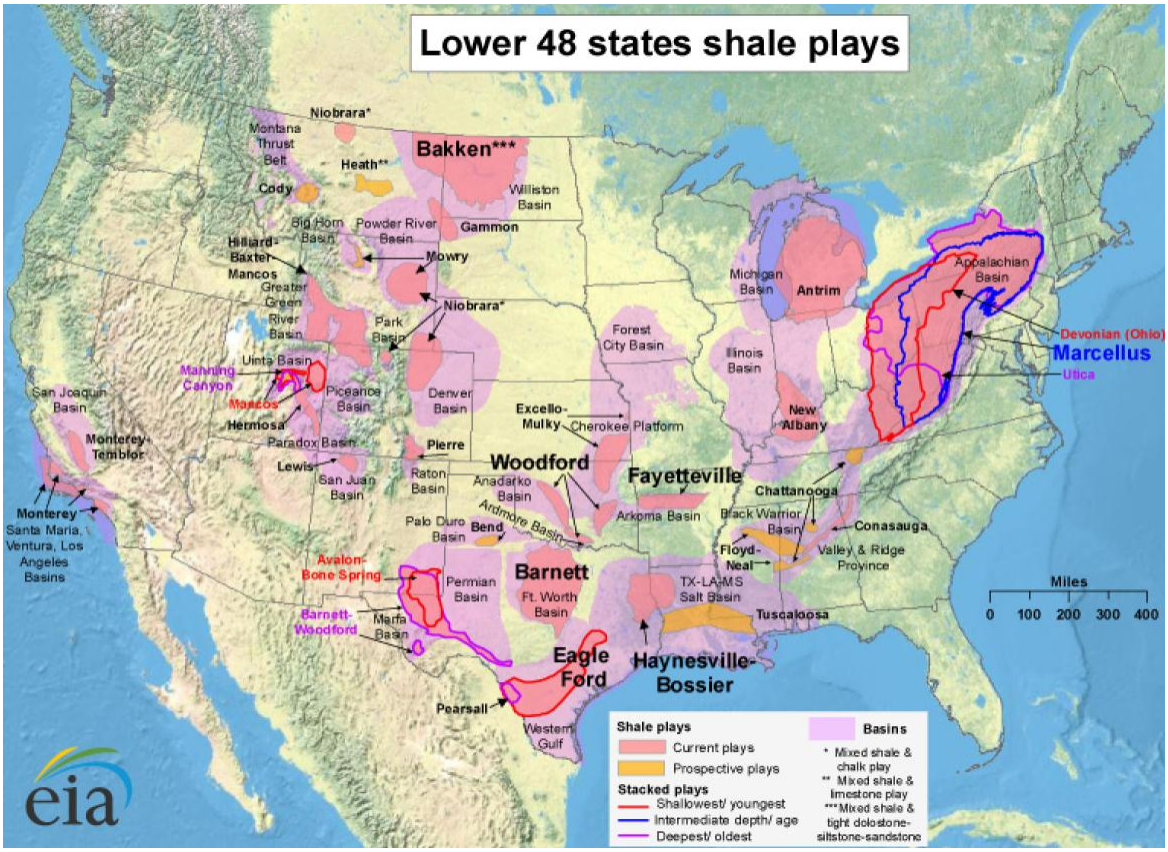

Figure 1.1 Map of U.S. shale gas and shale oil plays (as of May 9, 2011) (from U.S. Energy Information Administration).

biogenic types, and also thermogenic or combined biogenic-thermogenic gas accumulations (Curtis, 2002).

Shale reservoirs are commonly evaluated using five parameters, based on evidence from presently-producing shale formations: thermal maturity (shown as vitrinite reflectance), adsorbed gas fraction, reservoir thickness, total organic carbon content, and volume of gas in place (Curtis, 2002). The formation's productivity often relies on the degree of natural fractures and artificial fractures from stimulation (Curtis, 2002). Dry gas can only be produced from the most thermally mature shales, whereas wetter gas and

condensate comes from less thermally mature shales and oil from the least thermally mature shales (Frantz and Jochen, 2005).

THE WOODFORD SHALE

The Woodford Shale is a developing unconventional gas reservoir. The term resource shale describes the occurrence of all three parts of a petroleum system: a hydrocarbon source rock that acts as a source, seal and reservoir in a single unit. The presence, although not necessarily the producibility, of hydrocarbons is the main characteristic of resource shales. Mineralogy in resource shales may vary from "pure" shale consisting of clay minerals, and production may come from a range of lithofacies, including chert, sandstone, dolostone and siltstone, many of which may be artificially fractured to promote production (Comer, 1991b). The Woodford Shale formation is Late Devonian to Early Mississippian in age, and it extends widely across the southern mid-continent of the United States, including parts of Oklahoma, West Texas and New Mexico (Comer, 1991a). The Woodford Shale is one of several Devonian black shales in North America under exploration or development of shale gas (Harris, 2011). Current estimates from the Energy Information Administration show 28 trillion cubic feet of natural gas equivalent still recoverable from the Woodford Shale. The Woodford is stratigraphically similar to several Devonian black shales in North America, including the Antrim Shale in the Michigan Basin, the Chattanooga and Ohio Shales in the Appalachian Basin, the New Albany Shale in the Illinois Basin, the Bakken Formation in the Williston Basin, and the Exshaw Formation in the Western Canada Basin (Meissner, 1978; Cluff et al., 1981; Roen, 1984; Burrowes and Krause, 1987).

Lithofacies

The Woodford consists of two main lithofacies, black shale and siltstone. Other mixed lithologies, such as sandstone, chert, dolostone, mudstone and light-colored shale, also exist (Comer, 1991a). Four lithologies typically are associated with the significant potential gas production in the Woodford, and they vary by location. Those four lithologies are silty black shale in the Arkoma Basin in Oklahoma and Arkansas, chert in the frontal zone of the Ouachita fold belt in Oklahoma, siltstone and silty black shale in the Anadarko Basin in Oklahoma, siltstone and silty black shale in the Val Verde and Midland Basins in Texas, and silty black shale in the Delaware Basin in Texas and New Mexico (Comer, 2009).

Stratigraphy and Depositional Setting

The Woodford is principally Late Devonian in age, but ranges from Middle Devonian to Early Mississippian (Comer, 2009). The stratigraphic column which includes the Woodford in the Anadarko Basin, Oklahoma is shown in Figure 1.2. In Oklahoma, the Woodford unconformably overlies the Hunton group, but this is not the case in other basins. Above the Woodford is Mississippian limestone, a common formation in other basins. This study utilizes borehole well log data and surface seismic data located in Canadian County, Oklahoma (shown in Figure 1.3).

Source Rock and Maturity

The Woodford Shale's potential as a hydrocarbon source rock is based on its relatively high total organic carbon (TOC) content. In the realm of conventional oil, major resource plays of the world typically show TOC content greater than 2.5% by weight from the source rock (Jones, 1981). The Woodford contains mean organic carbon concentrations of 4.9% by weight in the Permian Basin (Texas and New Mexico), 5.7% by weight in the Anadarko Basin (Oklahoma and Arkansas), and 5.2% by weight for both

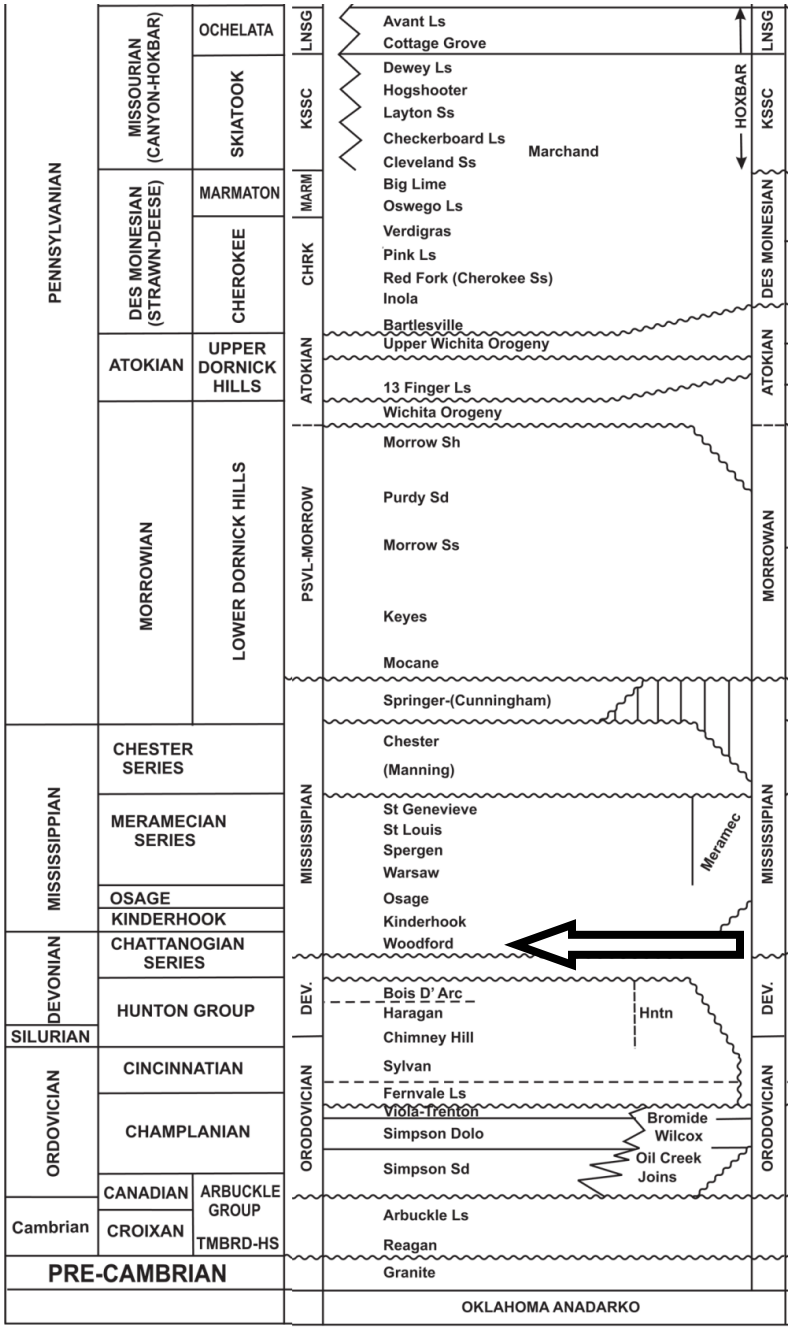

Figure 1.2 Stratigraphy of the lower Paleozoic section, including the Woodford Shale in the Anadarko Basin, Oklahoma (Harper, personal communication, 2011).

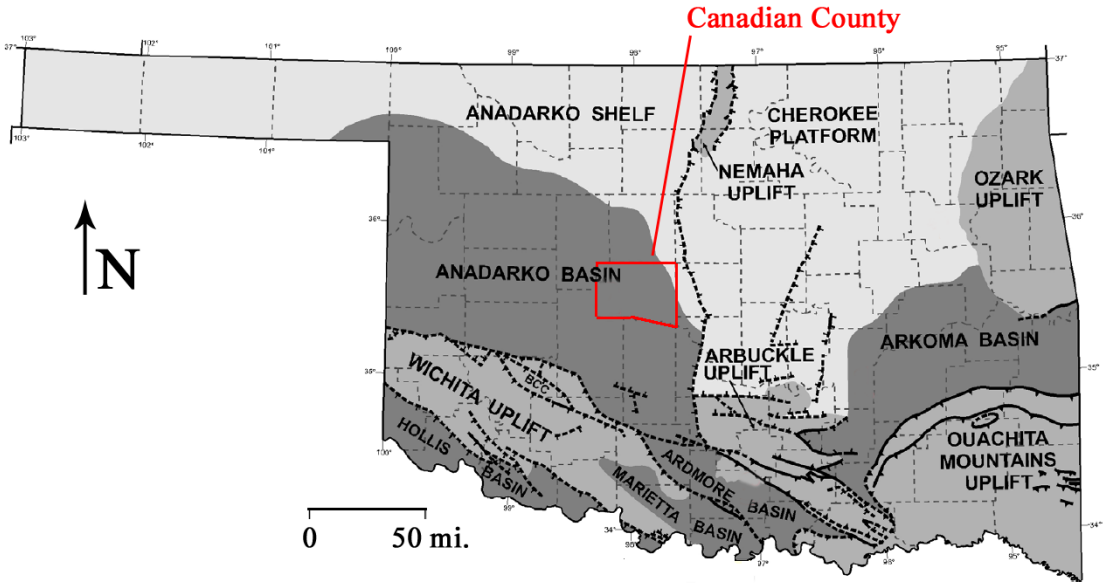

Figure 1.3 The location of the Anadarko Basin in western Oklahoma and Canadian County (highlighted in red). The Anadarko Basin is surrounded by the Anadarko Shelf, Arbuckle Uplift, Ardmore Basin, and Wichita Uplift (modified from Northcutt and Campbell, 1995).

regions combined (Comer, 2009). Such high values indicate the Woodford possesses higher TOC content than the sources of many major hydrocarbon accumulations. The maturity of the formation is estimated by measuring the vitrinite reflectance. The Woodford Shale shows a wide range of vitrinite reflectance: 0.7% to 4.89% (Boughal, 2008). In the Arkoma basin in eastern Oklahoma, the thermal maturity is more than 1.15% vitrinite reflectance in the dry gas window and less than 1.15% vitrinite reflectance in the oil window (Cardott, 2008). In the Anadarko Basin, from northeast to southwest, the average vitrinite reflectance increases from 0.51% to 2.6%, showing an increasing trend of thermal maturity (Lambert, 1982).

Fractures

The Woodford's fracture characteristics and regional patterns are important to the development and production of the shale. The sources of these natural fractures in the Woodford may be mechanical properties such as high brittleness (an attribute that indicates a rock's fracability), overburden and basal stresses, and its tectonic setting near major and minor faults. A study of fracture patterns at the surface using LIDAR data in a quarry in southeastern Oklahoma showed the Woodford shale to possess numerous fractures in the upper parts of the formation (Portas and Slatt, 2010). Outcrops proximal to this study also indicated the presence of natural fractures (Andrews, 2009). Shown in Figure 1.4a-b, the Woodford is composed of interbedded cherty and shale beds, where the fractures exist widely perpendicular to the bedding in the cherty layers but dissipate in the bounding shale; also shown is the black to grey fissile shale.

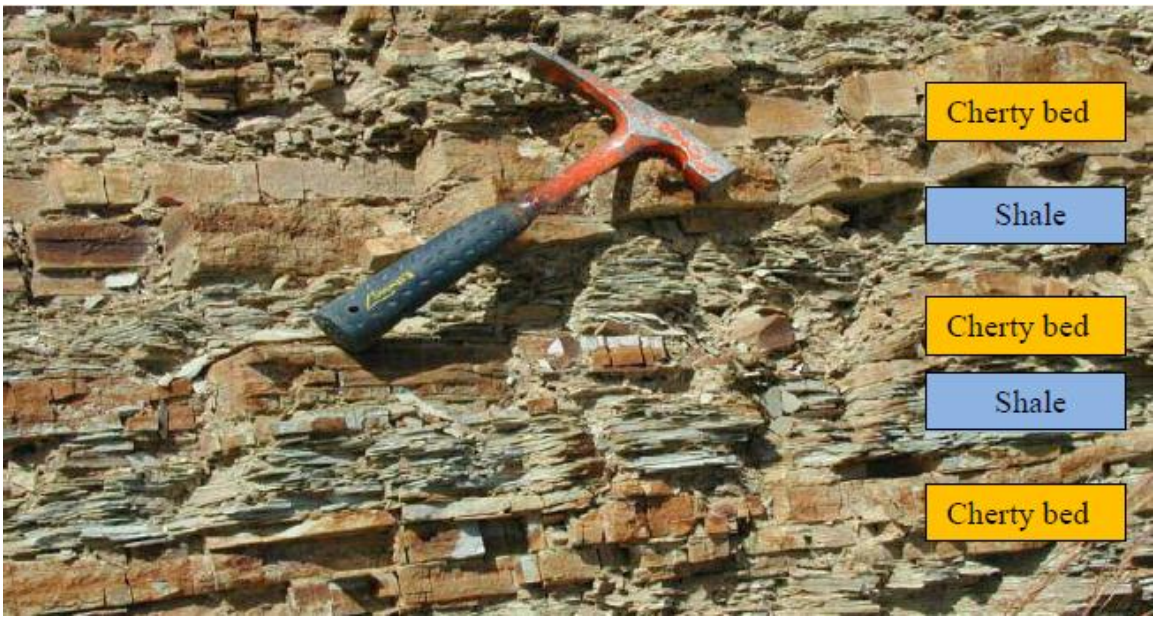

Figure 1.4a Alternating cherty and shale layers shown in the Woodford Shale, with fractures dissipating in bounding shale (Andrews, 2009).

Figure 1.4b Fissile shale shown in the Woodford (Andrews, 2009).

Hydrocarbon Production

The success of production in the Woodford Shale is primarily due to its high hydrocarbon content and potential for hydraulic fracturing. According to Rickman et al., (2008) brittleness is characterized by a weighted average of Poisson's ratio and Young's modulus. Using this definition, a lower value of Poisson's ratio (contributing to rock failure under stress) and a higher Young's modulus (contributing to maintaining fractures) would give a high brittleness value and the Woodford has shown higher values (Aoudia et. al, 2009). The brittleness of the Woodford, possibly due to richness in silicates, allows hydraulic fracturing to stimulate natural fractures and induce new ones. These fractures, either natural or induced, allow gas trapped by low permeability to migrate to the borehole from the tight formation. Production in the Woodford began in the 1930s with conventional (vertical) drilling (Boughal, 2008), but horizontal wells began in 2004 and have completely overtaken vertical wells. More than 300 horizontal Woodford Shale wells have been completed just in the Anadarko Basin since 2008 (Caldwell, 2011).

DATA UTILIZED

Both borehole well log data and surface seismic data were employed for this study of the Woodford. The 3-D 3-C seismic survey encompasses an area of the Anadarko Basin in Canadian County, Oklahoma. The survey is rectangular in shape, spanning about 14 square miles (2.7 miles E-W and 5.3 miles N-S). The survey was recorded with 3-component geophones, allowing for the measurement of both P-waves and converted P-S waves, although the vertical component P-P wave data were the primary source in this study. Both pre-stack and post-stack data were employed. Figure 1.3 shows the location of the Anadarko Basin and Canadian County.

The borehole well log data came from two wells both inside and outside of the seismic survey area. The one well within the survey area was the primary borehole information used here. The well data included standard log suites: sonic, gamma ray, resistivity, density, neutron porosity, as well as dipole sonic logs and mineralogical measurements from neutron-induced elemental gamma ray spectroscopy. The logged depths include many formations to the depth of 13,418 ft. (deeper than the Woodford in this location). A third well log was provided, but does not reach Woodford depths. The Woodford Shale in this area is approximately 13,000 ft. deep and 275 ft. thick, overlain by Mississippian limestone and overlying the Hunton Limestone.

OBJECTIVES

The objective of this study is to investigate the anisotropy present in the Woodford Shale by characterizing the natural fractures in the shale using both surface seismic techniques and rock physics modeling based on borehole data. An important feature of these low porosity, low permeability shale and tight rock formations are natural fractures, which impact hydraulic fracturing programs and subsequent production. Characterizing the orientation and density of a reservoir's natural fractures or stress fields requires both measurements from monopole and dipole sonic well logs and from surface seismic data. Dipole sonic measurements interact with the formation at a frequency of 2-10 kHz and this, along with other borehole logs, are useful for measuring P- and S-wave velocities and subsequently calculating details such as clay content and density. However, the log frequency has a limited volumetric sampling range away from the borehole (at the meter scale) due to wavelength considerations and may not characterize volumetric properties such as fracture density and dominant fracture orientation with the

necessary sampling or accuracy. The seismic data and its longer wavelengths (at the scale of 10's of meters) may help to resolve these larger scale properties. Specifically, this work investigates the Woodford Shale formation in the Anadarko Basin in western Oklahoma for horizontal transverse isotropy due to natural vertical fractures, which may be spaced at the scale of meters to 10's of meters.

From the seismic data, we can discern the orientation and relative crack density from amplitude varying with angle and azimuth (AVAZ) methods. While these results will be useful in and of themselves, the crack density shown is relative in a spatial sense. Initial analysis of the dipole sonic measurements of P- and S-wave velocities indicated the presence of vertical transverse isotropy (VTI) and no significant horizontal transverse isotropy (HTI). This VTI result may not be surprising given the natural layering at sub-meter scales and clay content of most shale. Analysis of seismic data using AVAZ methods, however, indicated that the Woodford does indeed possess HTI at seismic wave scales, further supporting the usefulness of seismic data to complete the characterization of these shale reservoirs. AVAZ methods have been used by numerous authors to investigate fracture parameters (Gray and Head, 2000; Hall and Kendall, 2000; Li, 1999; Lynn et al., 1996; MacBeth and Lynn, 2001; Montoya, 2002b; Pérez, 1999). Results from AVAZ analysis give the azimuthal orientation and the relative fracture intensity. To further characterize the fractures, a rock physics model is discussed that can serve as the basis for quantifying an absolute fracture density. From a rock physics model that generates a complete stiffness tensor, we can compare the seismic response from varying the crack density of the model to the field seismic data and therefore can attempt to map the relative density to an actual scaled density. Knowledge of both fracture density (the number of fractures with an average aspect ratio per unit volume) and fracture orientation, expressed as the dominant azimuthal direction, may contribute to productive

exploitation of the Woodford. Ideally, a horizontal drilling and hydraulic fracturing program would cross normal to higher-density areas of fractures to improve permeability and therefore production. Higher permeability maximizes effectiveness of these drilling and fracking programs (Wylie, 2007).

Modeling of this formation was initially performed by estimating the mineral composition and lithology of the Woodford from borehole log measurements. Starting with this background as an isotropic block, the method of Hashin-Shtrikman-Walpole bounds (Berryman, 1995) was performed to estimate values of rock stiffnesses at formation porosity, verified by other borehole measurements. Now working with an isotropic model including porosity, cracks were introduced to the model using the Hudson (1980) crack model, while again being constrained by dipole sonic measurements. Finally, fluid saturation was included in the model through the method of Brown and Korringa (1975). Through the combination of these petrophysical methods, a model of the anisotropic Woodford Shale was characterized by explicit composition, fracture parameters, and fluid saturation. Analysis of this computed stiffness tensor allowed for the synthesis of seismic data using ANIVEC (Mallick and Frazier, 1988) and analytic solutions for AVAZ results to be compared with AVAZ results from field seismic data. This will allow AVAZ results to now characterize a numeric fracture density. Obtaining the parameters that most significantly affect the AVAZ results will help develop a better understanding of the anisotropy in the Woodford.

THESIS ORGANIZATION

This thesis is divided into eight chapters. Chapter I provides a brief overview of current gas shale production, the Woodford Shale, and the study area involved in western

Oklahoma, USA. Chapter II covers the theories and methods of anisotropy, which builds a framework for the rest of the chapters in this study. Chapter III discusses the well log data available and the presence of VTI it suggests. Chapters IV and V cover the background to the amplitude varying with angle and azimuth (AVAZ) method and its application to the field seismic data, respectively. These chapters discuss the presence of HTI in the Woodford Shale. Chapter V deals exclusively with AVAZ results from the surface seismic survey and does not integrate any results or details from rock physics modeling. Chapter VI introduces the methods used in building the rock physics model in four parts (and its results) to demonstrate its reliability in describing the Woodford Shale going forward. Chapter VII discusses applying AVAZ to the rock physics model and mapping numeric fracture densities to the results from Chapter V using field seismic data. Chapter VIII covers discussions and conclusions from this work.

Chapter II: Anisotropy Background and Fundamentals

INTRODUCTION

The term anisotropy is used to describe a material's properties being directionally dependent. In other words, there are differences in the material's measured parameters based on the seismic wave propagation and/or polarization direction (as opposed to isotropy: identical properties in all locations). The existence of anisotropy, usually simplified as due to fractures or thin, periodic layers in either the horizontal and/or vertical directions, has measureable effects on a material's elastic stiffness and seismic velocity. If not correctly addressed, anisotropy has been shown to affect interpretation results of seismic data (Cheadle et al., 1991; Tatham et al., 1992). If an affected parameter is measured in different directions, properties of the fractured medium can be inferred. The location and density of these fractures has a large impact on the success of a drilling and fracturing completion operation and reservoir exploitation, as these fractures may be conduits for fluid flow. Two idealized types of anisotropy are discussed here: vertical transverse isotropy (VTI) where the axis of symmetry is vertical, due perhaps to horizontal bedding or aligned clay minerals, and horizontal transverse isotropy (HTI) where the axis of symmetry is horizontal due perhaps to vertical fracturing (Figure 2.1). Azimuthal anisotropy is known to prefer a certain azimuthal orientation due to regional horizontal stresses in basins forcing crack closures in certain azimuths (Mueller, 1992).

Investigation of shear waves show that birefringence (splitting) of the shear wave due to anisotropy could be related to fracture intensity and orientation (Tatham and McCormack, 1991). Shear waves traveling through an anisotropic medium will polarize into two directions: parallel to the predominant fracture direction (S1) and orthogonal to

this direction (S2). S1 is seen to have a higher velocity than S2. Currently, S1 and S2 are measured by dipole sonic borehole logs by recording arrival times azimuthally around the sonde.

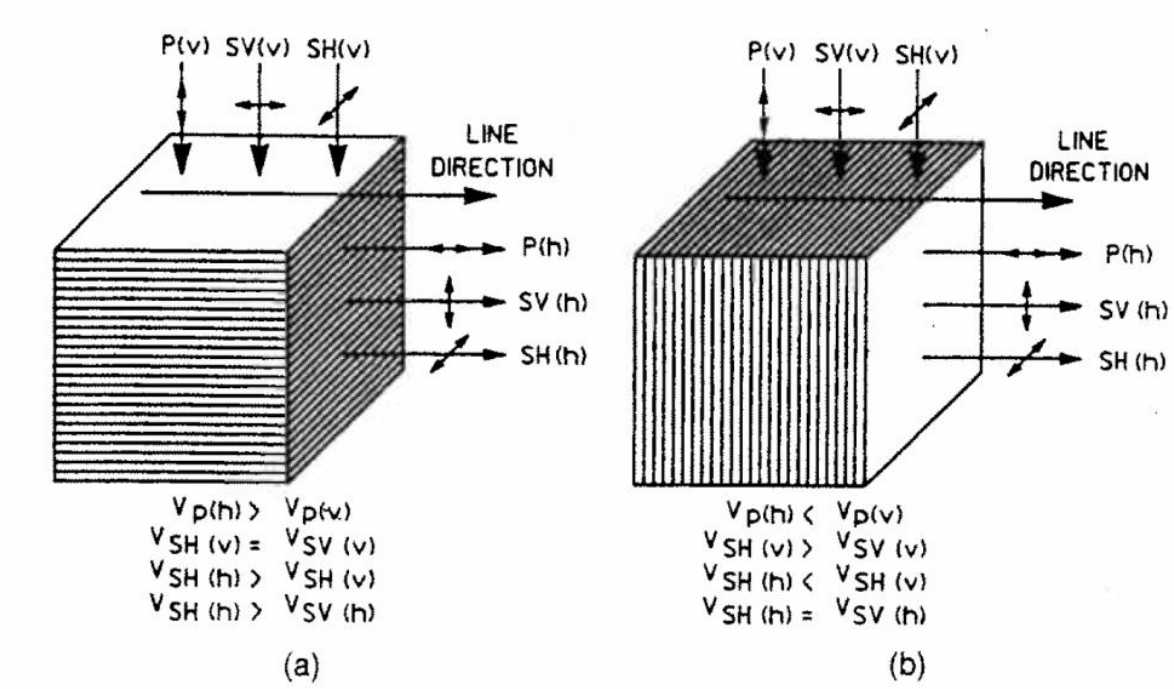

Figure 2.1 Examples of transverse isotropy. a) Vertical transverse isotropy (VTI) has a faster horizontal propagating P-wave velocity b) Horizontal transverse isotropy (HTI) shows S1 (SH(v)) polarization as faster than S2 (SV(v)) polarization (Tatham and McCormack, 1991).

Tensor Notation

According to Hooke's Law, for effective media with linear elastic solid properties, the stress is proportional to the strain and is expressed by the tensor relation:

$$\sigma_{ij} = C_{ijkl}\epsilon_{kl} \ , \tag{2.1}$$

where σ_{ij} is a rank 2 stress tensor, ϵ_{kl} is a rank 2 strain tensor and C_{ijkl} is a rank 4 stiffness tensor, or the constant of proportionality between stress and strain. C_{ijkl} is a fourth-ranked tensor with 81 components. Due to the symmetry conditions of the stress and strain tensors and some geometric considerations, it is represented by 21 independent elements. The stress (σ_{ij}) and strain (ϵ_{kl}) tensors can also be simplified in an abbreviated form with six independent components in the column stress and strain tensors T and E:

$$T = \begin{bmatrix} \sigma_1 = \sigma_{11} \\ \sigma_2 = \sigma_{22} \\ \sigma_3 = \sigma_{23} \\ \sigma_4 = \sigma_{23} \\ \sigma_5 = \sigma_{13} \\ \sigma_6 = \sigma_{12} \end{bmatrix} \qquad E = \begin{bmatrix} \epsilon_1 = \epsilon_{11} \\ \epsilon_2 = \epsilon_{22} \\ \epsilon_3 = \epsilon_{23} \\ \epsilon_4 = 2\epsilon_{23} \\ \epsilon_5 = 2\epsilon_{13} \\ \epsilon_6 = 2\epsilon_{12} \end{bmatrix} \tag{2.2}$$

The subscripts of the stiffness tensor C_{ijkl} can be replaced i(j) by $c_{ij} = C_{ijkl}$ in each pair of indices ij (kl) with the relations:

ij (kl)	i(j)
11	1
22	2
33	3
23, 32	4
13, 31	5
12, 21	6

In this way, $c_{ij}(6,6)$ is substituted for $C_{ijkl}(3,3,3,3)$. The stiffness tensor thus simplifies to a 6x6 matrix (Auld, 1973).

The stiffness tensor c_{ij} is expressed as follows for different anisotropies:

Isotropic Media:

$$c_{ij} = \begin{bmatrix} c_{11} & c_{12} & c_{12} & 0 & 0 & 0 \\ c_{12} & c_{11} & c_{12} & 0 & 0 & 0 \\ c_{12} & c_{12} & c_{11} & 0 & 0 & 0 \\ 0 & 0 & 0 & c_{44} & 0 & 0 \\ 0 & 0 & 0 & 0 & c_{44} & 0 \\ 0 & 0 & 0 & 0 & 0 & c_{44} \end{bmatrix} \tag{2.3}$$

Here $c_{12} = c_{11} - 2c_{44}$ and therefore, c_{ij} has a total of two independent elements.

VTI and HTI Media:

Figure 2.1 shows the simplified configurations of VTI and HTI anisotropic models, where the symmetry axis of the VTI model is in the x_3 direction and the symmetry axis of the HTI model is in the x_1 direction. The stiffness tensors of VTI and HTI media can be written as the following matrices (Musgrave, 1970; Rüger, 2002):

$$c_{ij}(VTI) = \begin{bmatrix} c_{11} & c_{12} & c_{13} & 0 & 0 & 0 \\ c_{12} & c_{11} & c_{13} & 0 & 0 & 0 \\ c_{13} & c_{13} & c_{33} & 0 & 0 & 0 \\ 0 & 0 & 0 & c_{55} & 0 & 0 \\ 0 & 0 & 0 & 0 & c_{55} & 0 \\ 0 & 0 & 0 & 0 & 0 & c_{66} \end{bmatrix} \tag{2.4}$$

Here $c_{12} = c_{11} - 2c_{66}$ and therefore, c_{ij} has a total of five independent elements.

$$c_{ij}(HTI) = \begin{bmatrix} c_{11} & c_{13} & c_{13} & 0 & 0 & 0 \\ c_{13} & c_{33} & c_{23} & 0 & 0 & 0 \\ c_{13} & c_{23} & c_{33} & 0 & 0 & 0 \\ 0 & 0 & 0 & c_{44} & 0 & 0 \\ 0 & 0 & 0 & 0 & c_{55} & 0 \\ 0 & 0 & 0 & 0 & 0 & c_{55} \end{bmatrix} \quad (2.5)$$

Here $c_{23} = c_{33} - 2c_{44}$ and therefore, c_{ij} has a total of five independent elements.

ELASTIC MEDIA

Isotropic Media

The term isotropic, as stated previously, signifies measurement is independent of measurement direction; regardless of the axis, the property measured is invariant with direction. This is different than the term homogenous, however, which means having uniform structure or composition with respect to location. While homogenous media can be isotropic media and vice versa, it is not required. In the case of velocity in an isotropic media, both the propagation and polarization direction of a wave has no effect.

The Zoeppritz (1919) equations were developed to understand the reflection and transmission modes of seismic wave propagation through isotropic media at discontinuities in elastic parameters and density. Based on these equations, Aki and Richards (1980), Shuey (1985), Hilterman (1989), and Thomsen (1990) have approximated the linear forms of the P-P wave reflection amplitude versus offset (AVO) equations and most approximations are valid from 0 to 30 degrees incidence angle. These approximations agree well with the Zoeppritz equations in this angle range, for small contrasts in elastic parameters and density, and are used extensively in analysis of surface seismic data. Using assumptions of small impedance contrasts between two layers, the

equations simplify further to incorporate terms commonly used such as V_p/V_s ratio, Poisson's ratio, and AVO intercept and gradient.

The AVO technique for P-P reflections became widely applied after Ostrander (1982, 1984) published preliminary results. Four classes of AVO (Rutherford and Williams, 1989; Castagna and Swan, 1997) responses have been introduced to distinguish sandstones with liquid and gas saturation. It has become a popular tool as a direct hydrocarbon (gas) indicator, but because it is based on approximation equations in the isotropic case, its usefulness may be somewhat limited to the cases of low gas saturation and tight shales.

The compressional and shear propagation velocities (V_p, V_s) of isotropic media are expressed as follows:

$$V_p = \sqrt{\frac{\lambda+2\mu}{\rho}} \tag{2.6a}$$

$$V_s = \sqrt{\frac{\mu}{\rho}} \tag{2.6b}$$

Here λ and μ are the Lamé constants and ρ is the density of the isotropic media. The equation (2.3) for isotropic cases is rewritten as such:

$$c_{ij} = \begin{bmatrix} \lambda+2\mu & \lambda & \lambda & 0 & 0 & 0 \\ \lambda & \lambda+2\mu & \lambda & 0 & 0 & 0 \\ \lambda & \lambda & \lambda+2\mu & 0 & 0 & 0 \\ 0 & 0 & 0 & \mu & 0 & 0 \\ 0 & 0 & 0 & 0 & \mu & 0 \\ 0 & 0 & 0 & 0 & 0 & \mu \end{bmatrix} \tag{2.7}$$

The compressional and shear velocities are rewritten as:

$$V_p = \sqrt{\frac{c_{11}}{\rho}} \tag{2.8a}$$

$$V_s = \sqrt{\frac{c_{44}}{\rho}} = \sqrt{\frac{c_{55}}{\rho}} \tag{2.8b}$$

VTI Media

A medium showing vertical transverse isotropy (VTI) is commonly pictured as a layering of individual isotropic layers with a vertical axis of symmetry (Figure 2.1). The existence of VTI does affect the velocity measurement dependent on wave propagation and polarization directions. For a vertically propagating S-wave, velocities of SH and SV are equivalent in each vertical layer (from Figure 2.1: $V_{SH}(v) = V_{SV}(v)$). For a P-wave, however, the velocities of waves which propagate horizontally are larger than those that travel along the vertical symmetry axis ($V_P(h) > V_P(v)$). These directionally-dependent measurements are expressed in the stiffness tensor using Lamé's constants as:

$$c_{ij}(VTI) = \begin{bmatrix} \lambda_{\parallel} + 2\mu_{\parallel} & \lambda_{\parallel} & \lambda_{\perp} & 0 & 0 & 0 \\ \lambda_{\parallel} & \lambda_{\parallel} + 2\mu_{\parallel} & \lambda_{\perp} & 0 & 0 & 0 \\ \lambda_{\perp} & \lambda_{\perp} & \lambda_{\perp} + 2\mu_{\perp} & 0 & 0 & 0 \\ 0 & 0 & 0 & \mu_{\perp} & 0 & 0 \\ 0 & 0 & 0 & 0 & \mu_{\perp} & 0 \\ 0 & 0 & 0 & 0 & 0 & \mu_{\parallel} \end{bmatrix} \tag{2.9}$$

Here $\lambda_{\parallel}$ and $\mu_{\parallel}$ are the Lamé constants which are in the direction parallel to the horizontal layers, $\lambda_{\perp}$ and $\mu_{\perp}$ are the Lamé constants which are in the direction parallel to the symmetry axis.

Constraints similar to Equation 2.4 exist for this expression and are as follows (Auld, 1973; Berge, 1995):

$$c_{11} \geq c_{66} \geq 0$$

$$c_{33} \geq 0$$

$$c_{44} \geq 0$$

$$(c_{13})^2 \leq c_{33}(c_{11} - c_{66})$$

Backus (1962) demonstrated that for finely-layered, horizontally-stratified, transversely isotropic elastic media, and with seismic wavelengths larger than the layer thickness, the elastic constants of each isotropic horizontal layer could be averaged to represent the anisotropic medium as a singular homogeneous medium. For this kind of anisotropy, additional constraints are applied (Backus, 1962; Berge 1995):

$$c_{33} > c_{13}$$

$$c_{33} > \frac{4}{3} c_{44}$$

$$c_{66} \geq c_{44}$$

Thomsen (1986) developed the concept of weak elastic anisotropy, which was seen by many investigators as describing bulk elastic media (10-20% of the media summarized from earlier papers). He derived the parameters ε, γ and δ (now known as Thomsen's parameters), which researchers find more intuitive to use than single elements of the stiffness tensor. Their expression in terms of tensor elements is:

$$Vp_{\perp} = \sqrt{\frac{c_{33}}{\rho}} \tag{2.10a}$$

$$Vs_{\perp} = \sqrt{\frac{c_{55}}{\rho}} \tag{2.10b}$$

$$\varepsilon = \frac{c_{11} - c_{33}}{2c_{33}} \approx \frac{Vp_{\parallel} - Vp_{\perp}}{Vp_{\perp}} \tag{2.11a}$$

$$\gamma = \frac{c_{66} - c_{44}}{2c_{44}} \approx \frac{Vs_{\parallel} - Vs_{\perp}}{Vs_{\perp}} \tag{2.11b}$$

$$\delta = \frac{(c_{13} + c_{44})^2 - (c_{33} - c_{44})^2}{2c_{33}(c_{33} - c_{44})} \tag{2.11c}$$

Here $Vp_{\perp}$ and $Vs_{\perp}$ are the P-wave velocity and S-wave velocity, respectively, traveling along the vertical symmetry axis. $Vp_{\parallel}$ is the P-wave propagating orthogonal to the vertical symmetry axis (horizontally). $Vs_{\parallel}$ is the fast shear wave velocity traveling in the horizontal direction and polarized in the horizontal direction, and $Vs_{\perp}$ (2.11b) is the slow shear wave velocity traveling vertically but polarized along the horizontal layer (equivalent to the shear wave propagating horizontally and polarized in the vertical plane) (Mavko et al., 2009).

Compared with equations (2.9), (2.4) and (2.8a-b), ε is often expressed as the degree of P-wave anisotropy, due to the difference between c_{11} and c_{33}, or $Vp_{\parallel}$ and $Vp_{\perp}$ propagating horizontally and vertically. We know from equation (2.9) that c_{11} represents the P-wave velocity propagating parallel to the horizontal layers and c_{33} gives the P-wave velocity propagating parallel to the vertical symmetry axis. The Thomsen parameter γ (Equation 2.11b) is expressed as the degree of S-wave anisotropy. For weak anisotropy, Thomsen also points out that δ is an important indicator of anisotropy, but it is not as readily intuitive. Weak anisotropy is usually described as ε, γ and δ << 1. Thomsen

(1986) investigated commonly used sedimentary rocks (such as Mesaverde sandstones and shales) from multiple researchers and concluded that most of these rocks have anisotropy in the weak-to-moderate range (< 0.2).

For simplified cases, elliptically anisotropic media have the character $\delta=\varepsilon$ (Daley and Hron, 1979; Thomsen, 1986). If anisotropy in the rock is caused by fine layering of isotropic materials, $\delta<\varepsilon$ (Berryman, 1979; Helbig, 1979; Thomsen, 1986). According to equations (2.4), (2.9), and their corresponding constraints, it was shown that $\varepsilon > 0$ and $\gamma > 0$ in VTI media. The parameter δ can be either positive or negative.

HTI Media and Equivalent Thomsen Parameters

A medium showing horizontal transverse isotropy (HTI) is commonly pictured as a layer with aligned vertical fractures and a horizontal symmetry axis (Figure 2.1). The existence of HTI does affect the velocity measurement dependent on both wave propagation and polarization directions. For a vertically propagating S-wave, the fractures cause the wave to split into SV and SH, which now have differing velocities. In this case, the horizontally polarized SH wave travels parallel to the fractures and the SV wave polarized in the vertical plane propagates perpendicular to the fractures, therefore the SH wave would be faster ($V_{SH}(v) > V_{SV}(v)$ in Figure 2.1). In general, the wave splits into two directions, generating a wave called the fast shear wave, or S1, that travels and is polarized in the isotropic vertical plane (parallel to fractures), and the slow shear wave, or S2, that propagates parallel to the fractures but is polarized perpendicular to the fractures. For a vertically propagating P-wave, its velocity travels along the vertical isotropic plane and its velocity is larger than that which propagates along the horizontal symmetry axis direction. The stiffness matrix using Lamé constants is derived from equation (2.5) and is shown:

$$c_{ij}(HTI) = \begin{bmatrix} \lambda_\perp + 2\mu_\perp & \lambda_\perp & \lambda_\perp & 0 & 0 & 0 \\ \lambda_\perp & \lambda_\parallel + 2\mu_\parallel & \lambda_\parallel & 0 & 0 & 0 \\ \lambda_\perp & \lambda_\parallel & \lambda_\parallel + 2\mu_\parallel & 0 & 0 & 0 \\ 0 & 0 & 0 & \mu_\parallel & 0 & 0 \\ 0 & 0 & 0 & 0 & \mu_\perp & 0 \\ 0 & 0 & 0 & 0 & 0 & \mu_\perp \end{bmatrix} \tag{2.12}$$

Here $\lambda_\parallel$ and $\mu_\parallel$ are the Lamé constants which are in the direction parallel to the vertical fractures, $\lambda_\perp$ and $\mu_\perp$ are the Lamé constants which are in the direction parallel to the horizontal axis.

Similar anisotropy parameters in equation (2.11) have been derived to represent the physical meanings for HTI media (Rüger, 1995,1996; Chen, 1995; Mavko, 2003).

$$Vp_\parallel = \sqrt{\frac{c_{33}}{\rho}} \tag{2.13a}$$

$$Vs_\parallel = \sqrt{\frac{c_{44}}{\rho}} \tag{2.13b}$$

$$Vs_\perp = \sqrt{\frac{c_{55}}{\rho}} \tag{2.13c}$$

$$\varepsilon^{(v)} = \frac{c_{11} - c_{33}}{2c_{33}} \approx \frac{Vp_\perp - Vp_\parallel}{Vp_\parallel} \tag{2.14a}$$

$$\gamma^{(v)} = \frac{c_{66} - c_{44}}{2c_{44}} \approx \frac{Vs_{\perp} - Vs_{\parallel}}{Vs_{\parallel}} \tag{2.14b}$$

$$\delta^{(v)} = \frac{(c_{13} + c_{55})^2 - (c_{33} - c_{55})^2}{2c_{33}(c_{33} - c_{55})} \tag{2.14c}$$

Here $Vp_{\parallel}$ and $Vs_{\parallel}$ are the P-wave velocity and S-wave velocity, respectively, both traveling parallel to the vertical fractures. $Vs_{\parallel}$ is the S-wave polarized in the vertical isotropic plane traveling in the vertical direction. $Vs_{\perp}$ is the S-wave polarized along the symmetry axis and traveling vertically. The parameter $\varepsilon^{(v)}$ and $\gamma^{(v)}$ express the degree of anisotropy for P-waves and S-waves, similar to what was described in Thomsen's VTI parameters. Comparing equations (2.12) with (2.5), the elastic constants parallel to the factures are larger than that perpendicular to the fractures. Therefore, it was shown that $\varepsilon^{(v)}$ and $\gamma^{(v)}$ are both negative. $\delta^{(v)}$ can be either positive or negative. The HTI parameters are related to the equivalent VTI media parameters (Rüger, 2002):

$$\varepsilon^{(v)} = -\frac{\varepsilon}{1 + 2\varepsilon} \tag{2.15a}$$

$$\gamma^{(v)} = -\frac{\gamma}{1 + 2\gamma} \tag{2.15b}$$

$$\delta^{(v)} = \frac{\delta - 2\,\varepsilon\left(1 + \frac{\varepsilon}{f}\right)}{(1 + 2\varepsilon)\left(1 + \frac{2\varepsilon}{f}\right)} \tag{2.15c}$$

$$f = 1 - \left(\frac{V_{S0}}{V_{P0}}\right)^2 \tag{2.15d}$$

Here V_{S0} and V_{P0} are velocities measured along the horizontal axis. ε, γ and δ are Thomsen's parameters discussed in equation (2.11a-c). The HTI parameters should also satisfy: $\varepsilon^{(v)}$, $\gamma^{(v)}$ and $\delta^{(v)} << 1$.

ANISOTROPIC EFFECT ON AVO

Rüger (2002) shows that HTI anisotropy does have an effect on the AVO response as a function of azimuth. As this is integral to the understanding of the AVAZ method used in Chapter IV, a brief discussion on this topic will be reported there.

SUMMARY

This chapter provides a background summary of anisotropy and its relationship to observable quantities such as seismic velocity. Two common types of anisotropy are vertical and horizontal transverse isotropy, whose presence is determined by characteristics of P- and S-wave velocities in different polarization and propagation directions. Thomsen's parameters are introduced as an effective notation for describing anisotropy in an intuitive physical sense. Symmetry of the medium allows the description of VTI and HTI media with 5 independent constants only.

Chapter III: Borehole Geophysical Log Characteristics of the Woodford Shale, Anadarko Basin, Oklahoma

WELL LOG INFORMATION FOR THE WOODFORD SHALE

This portion of the study is based on borehole data from a vertical well drilled in Canadian County, Oklahoma. Although I do not have permission to disclose the exact geographical location of the well within the survey area, the well log data includes caliper, gamma ray, resistivity, density, neutron, sonic logs, as well as dipole sonic logs with shear wave velocities at various polarizations. Further, mineralogical logs describing the mineral composition of the formations are included. Because different well logs have different depth ranges, no single values are given for maximum depth of well log coverage (the well itself goes to 13,418 ft.). Gamma ray, for example, runs the depths from 216 ft. to 13,370 ft. The other logs used here also reach that depth, which is approximately 125 ft. below the base of the Woodford Shale. The sonic and dipole logs measure P and S-wave velocities from 10,680 ft. to 13,370 ft.

Some of the log data within the Woodford interval and the surrounding limestone formations are shown in Figure 3.1. Curves included are (from left to right) the gamma ray (GR), bulk density (ρ), P-wave velocity (Vp), S-wave velocity (Vs), P-wave S-wave ratio (Vp/Vs), bulk modulus (K) and shear modulus (μ). The values K and μ curves are calculated directly from V_p, V_s, and ρ. The Woodford Shale exists between 12973 and 13245 ft., and it is distinguishable in the GR, ρ, Vp, Vs, K, and μ logs. Above the Woodford formation sits Mississippian limestone and below sits the Hunton Limestone. In the Woodford, the average bulk density (ρ) is ~2.45 g/cm^3, while the average V_p is

~3.3 km/s and V_s is ~2 km/s. This low density has been observed by previous studies of organic black shales (Vernik and Nur, 1992; Vernik and Liu, 1997).

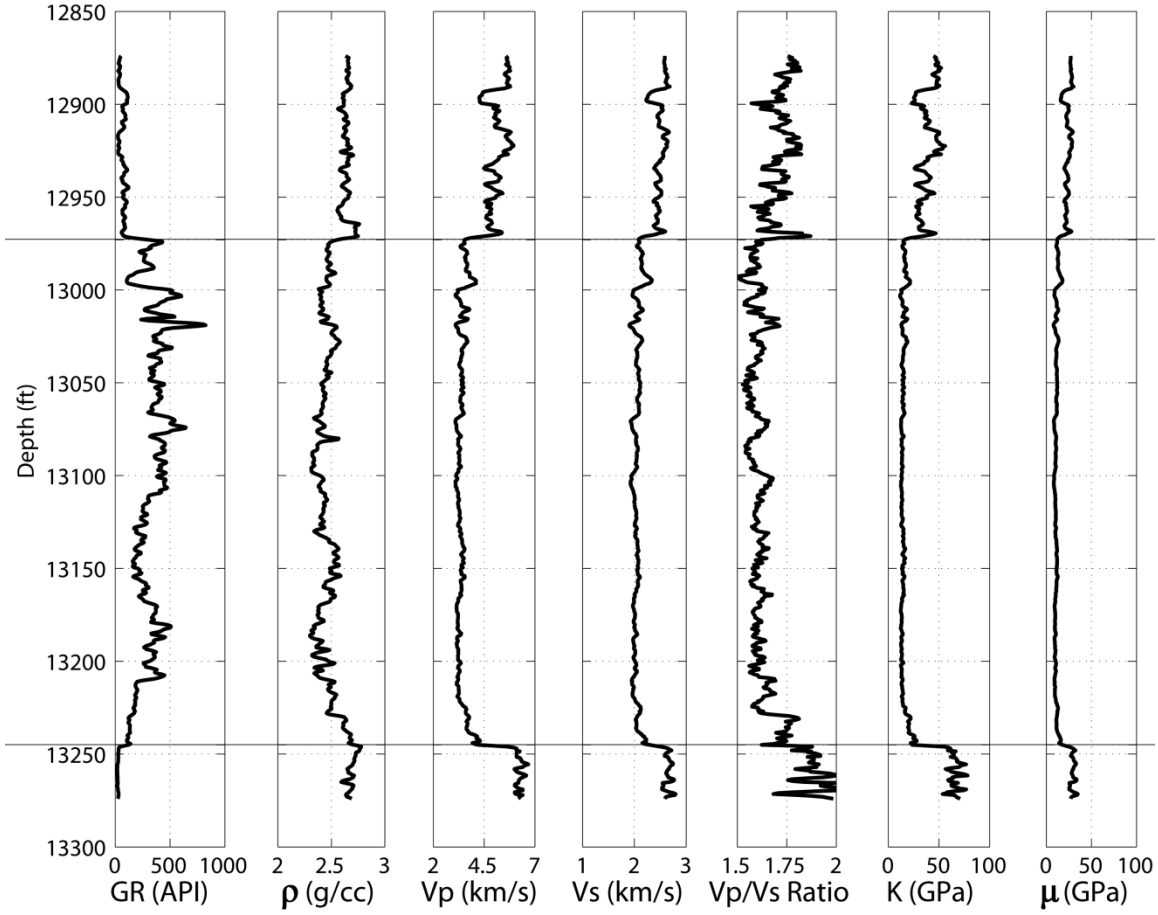

Figure 3.1 Well data that samples the Woodford Shale: the Woodford lies between 12973 and 13245 ft. depths. Well log curves are (left to right) gamma ray, bulk density, P-wave velocity, S-wave velocity, and calculated logs velocity (Vp/Vs) ratio, bulk modulus, and shear modulus.

An overview of the logs in the Woodford interval show little variation in the caliper log, which suggests the reliability of the measurement of other logs, especially the sonic log and dipole sonic logs, is good. Gamma ray response is strikingly high between the top and bottom of the Woodford and makes it easily discernible. This high response may be due to other catalysts, such as excessive uranium, but no spectral gamma ray log was present to correct for it. Regardless, the response was noticeable and allowed for easy interpretation of the formation boundaries at the top and base of the Woodford.

SUBDIVIDING THE WOODFORD SHALE

It is a common practice in studies of the Woodford Shale to divide the unit into subunits based on log signatures of resistivity, gamma ray response, and density (Ellison 1950; Hester et al., 1988, 1990). Other studies outside of geophysics have informally divided the Woodford into an "upper", "middle," and "lower" based on palynomorphs, an organic microfossil, (Urban, 1960; Von Almen, 1970) and geochemistry (Sullivan, 1985). While the distinctions usually found in log signatures are seen in this work's well log data, for this study it was unnecessary to divide the formation, as this work depends on seismic data that have reflections only representing the bulk Woodford character and top and bottom of the formation. An investigation of mineralogy in the Woodford Shale does show three distinct units (like previous studies postulate), but its importance will be discussed in Chapter VI regarding the composite estimate for rock physics modeling.

MINERALOGY OF THE WOODFORD SHALE

The mineralogy of the Woodford Shale comes from borehole log data responding to multiple elements and minerals using neutron-induced elemental gamma ray

spectroscopy. The resulting categories here fall into five elements: calcite, clay minerals, quartz, pyrite, and kerogen. A graph representing their respective percentages is shown in Figure 3.2. Dividing lines show the boundary of the top and bottom of the Woodford. With the bounding limestones on either side of the Woodford Shale, one would expect a high percentage of calcite outside of the formation, and that was seen clearly.

From this figure, we can observe the distinct differences between the Woodford (with large parts of clay minerals and quartz) and the surrounding limestones (Mississippian above and Hunton below), specifically the presence of kerogen and increase in clay content. A key observation from this mineralogy figure was the high level of quartz within the Woodford Shale. With alternating cherty layers between shale layers, it was not surprising however to see the formation be quartz rich. The higher siliceous quartz content in the Woodford has been shown to readily enhance fracturing (Guo et al., 2010) because of the increased rigidity and brittleness.

The ranges of values seen in the mineralogical logs are summarized in Table 3.1; these are average values over the formation:

	Lower Mississippian limestone	Woodford Shale	Upper Hunton Limestone
Calcite	33.2%	1.8%	80.4%
Clay	14.6%	33.8%	6.6%
Pyrite	1.5%	5.3%	0.8%
Quartz	50.5%	53.2%	12.1%
Kerogen	0.2%	5.9%	0.0%

Table 3.1 Average mineralogical values for the lower Mississippian limestone, Woodford Shale, and upper Hunton Limestone.

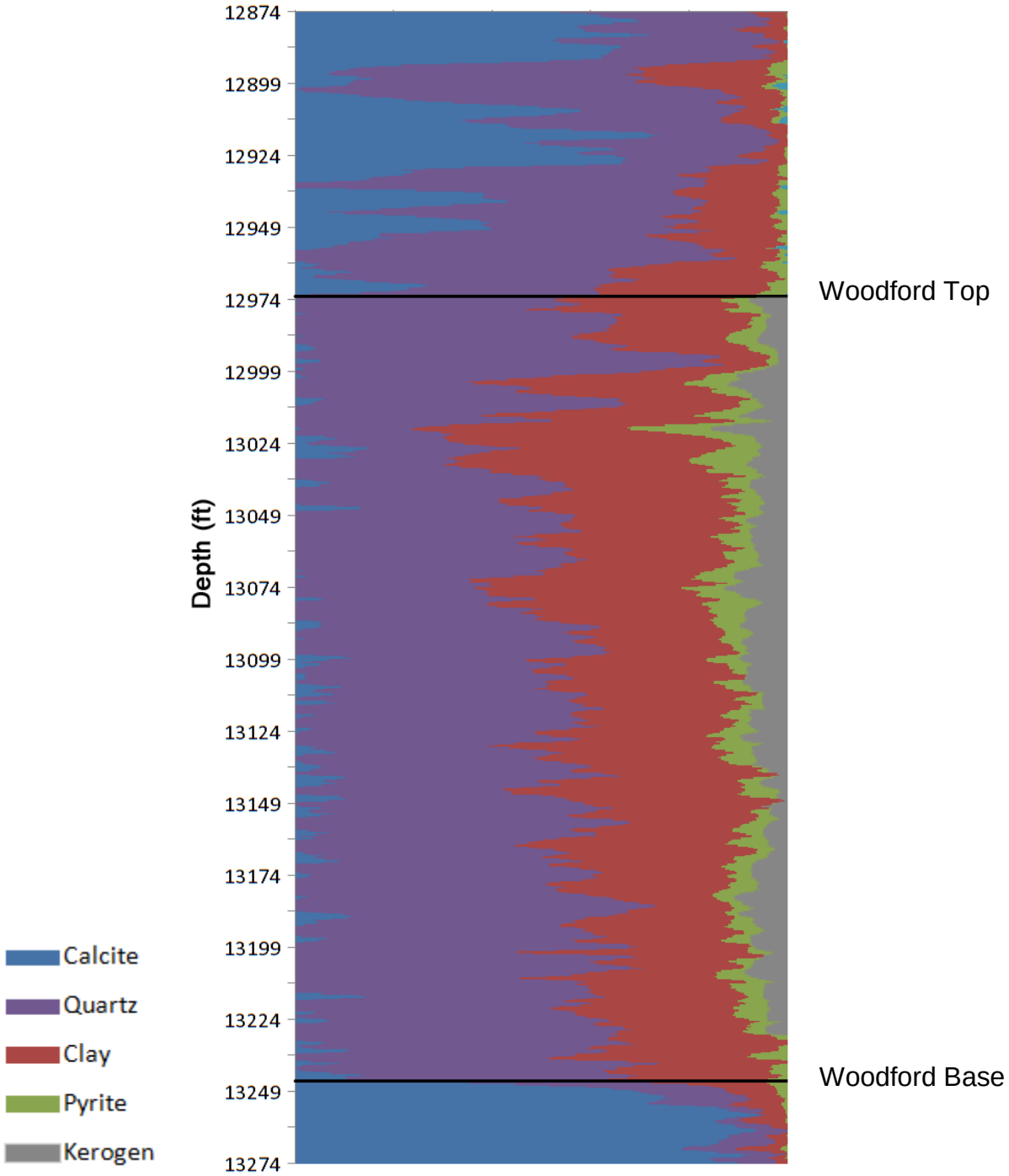

Figure 3.2 Mineralogy of the Mississippian limestone (upper section), Woodford Shale (middle section), and Hunton Limestone (lower section). Note the presence of kerogen, the relative absence of calcite, and relatively higher clay and quartz content of the Woodford Shale.

EVIDENCE FOR ANISOTROPY

The suite of calculations from the dipole sonic borehole logs was extensive, and included P-wave velocity for the horizontal propagation directions, as well as a fast and slow shear wave (S1 and S2) velocity in the horizontal polarization (vertical propagation) direction. The horizontal P-wave velocity was estimated from analysis of the Stoneley wave from the borehole boundary to extract the C_{11} stiffness tensor element (investigations into the details of this proprietary calculation were unsuccessful).

In a VTI medium, the horizontal P-wave velocity typically exceeds the vertical P-wave velocity, and there is negligible difference between the vertically propagating S1 and S2 velocities, as each horizontal bedding layer would be isotropic (Figure 2.1). In Figure 3.3, velocity data is shown. The curve titled 'Vp Diff' is the percentage difference between the vertically and horizontally propagating P-wave velocities, also known as the Thomsen parameter ε. Similarly with 'Vs Diff', this is the percentage difference between vertically propagating S1 and S2, also known as the Thomsen parameter γ. This figure demonstrates exactly what is expected in a VTI medium: namely the difference in vertically and horizontally propagating V_p is large and the difference in all polarizations of vertically propagating shear waves is negligible. With the Vp difference, we observe that the vertical (normal to bedding) P-wave velocity is lower, which has been observed before in organic black shales (Vernik and Nur, 1992; Vernik and Liu, 1997). In fact, due to the nature of bedding in shales, many properties, such as bulk modulus and P-wave velocity, are even assumed to behave as in a VTI medium (Brevik et al., 2007). While these borehole results are consistent with these assumptions, the seismic data, operating on an entirely different spatial resolution, showed further investigation was needed (see Chapter V).

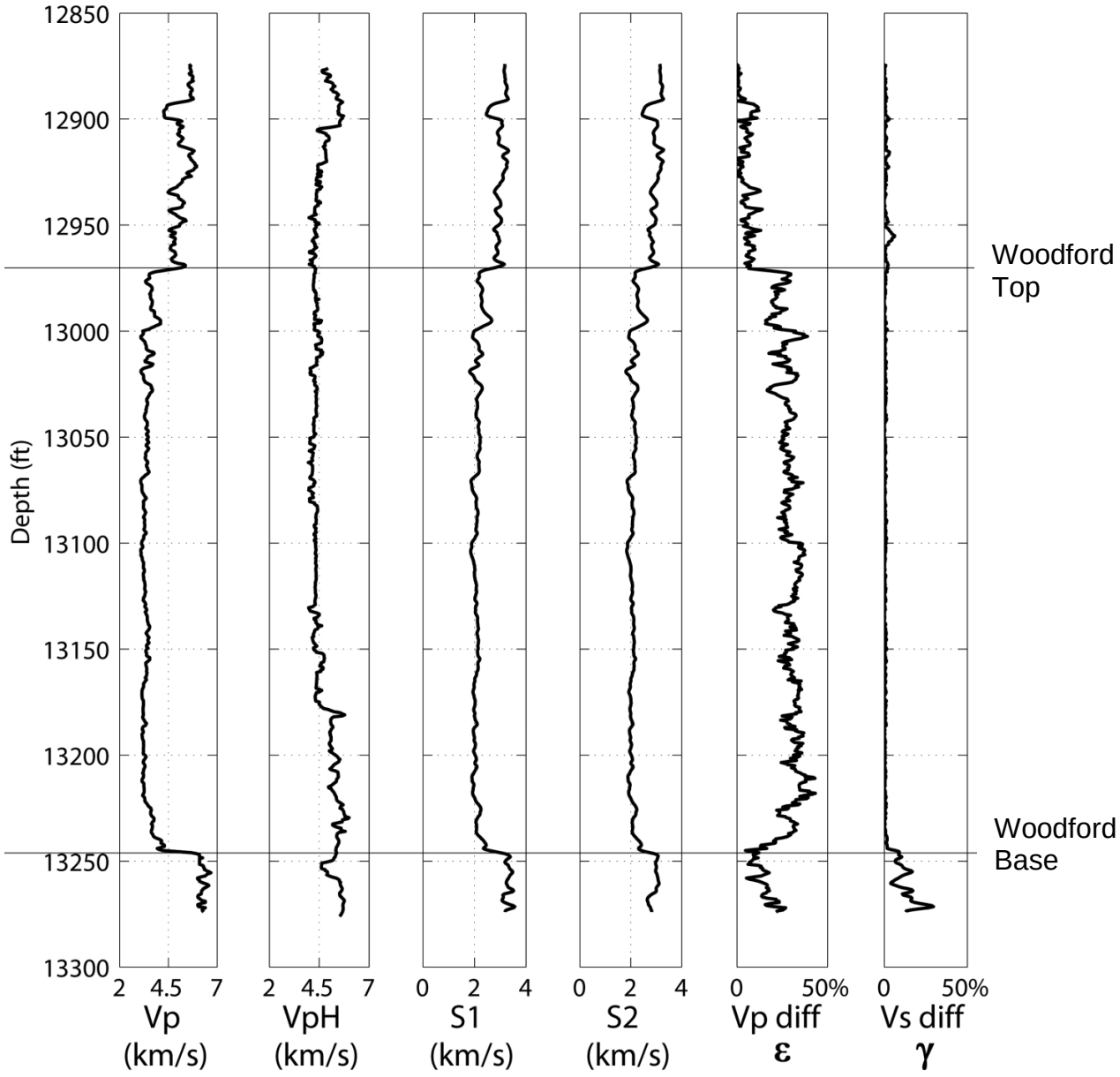

Figure 3.3 Well log data processed for specific velocities of the Woodford Shale. Logs, from left-to-right: vertically propagating P-wave velocity, computed horizontally propagating P-wave velocity, fast and slow vertically propagating shear wave velocity, difference between vertically and horizontally propagating P-wave velocity (Vp diff / ϵ), and difference between fast and slow shear waves (Vs diff / γ). Evidence for the presence of VTI is the difference in P-wave velocity and absence of HTI is the negligible difference in S-wave velocity, suggesting no observed effects of vertical fractures.

SUMMARY

This chapter described the well log measurements of the Woodford Shale and its bounding layers. From these measurements, the Woodford Shale is discernable with its high gamma ray response and decrease in seismic P- and S-wave velocities. The mineralogical content of these logs is important and serves as the basis for rock physics modeling done later. Analysis of the P- and S-wave velocities in the borehole indicated the presence of vertical transverse isotropy, which is studied further in later chapters. Obviously, the measurements from one well cannot describe the entire regional lithology and rock properties of the Woodford Shale and interpretations here can be improved with supplemental data.

Chapter IV: Amplitude Varying with Angle and Azimuth (AVAZ)

INTRODUCTION

P-wave reflection amplitudes are sensitive to azimuthal anisotropy induced by vertical fractures (HTI) and can be affected both as a function of source-receiver offset and azimuthal variations in source-receiver position. This investigation of amplitude varying with angle of incidence and source-receiver azimuth (AVAZ) allowed an estimation of orientation of vertical fractures and relative fracture density. Investigating reflection amplitudes has advantages over investigating traveltime differences because AVAZ concentrates on contrasts across a single reflecting surface, while traveltime methods are affected by propagation effects through overlying layers all the way to the surface (Hall and Kendall, 2000). Another advantage of AVAZ is the ability to detect fracture parameters using only vertical component P-wave data.

Fundamentally, AVAZ is a 3-D extension of varying reflection amplitudes with offset (AVO), which was summarized in detail by Castagna and Backus (1993), Ostrander (1982), and Rutherford and Williams (1989). Zoepprittz (1919) earlier described the full equations of P-wave reflectivity between two isotropic half-spaces, and then Shuey (1985) approximated these equations for small angles of incidence (θ < 35 degrees) with the formula:

$$Rp(\theta) = A + B\sin^2(\theta) + C\sin^2(\theta)\tan^2(\theta) \tag{4.1}$$

where $Rp(\theta)$ is the P-wave reflection coefficient at an incidence angle θ, A is the reflection coefficient at normal incidence (also known as AVO intercept), B is known as

the AVO gradient, and *C* is a third term that becomes important at larger angles. The AVO gradient *B* is a function of AVO intercept and contrasts in Poisson's ratio σ across the interface, which also is a function of the ratio of P-wave and S-wave velocities. These coefficients were further simplified by Thomsen (1990) as:

$$A = \Delta Z/(2\bar{Z}) \tag{4.2a}$$

$$B = \frac{1}{2}\left(\frac{\Delta V_p}{\bar{V}_p} - \frac{\left(\frac{2\bar{V}_s}{\bar{V}_p}\right)^2 \Delta\mu}{\mu}\right) \tag{4.2b}$$

$$C = 1/2\left(\frac{\Delta V_p}{\bar{V}_p}\right) \tag{4.2c}$$

where V_p is P-wave velocity, V_s is S-wave velocity, Z is the acoustic impedance (ρV_p) and μ is the shear modulus. Terms with a bar indicate the average values across the reflecting interface and Δ signifies the difference across the interface.

If the media contain no HTI azimuthal anisotropy, the AVO terms will be equal for all azimuthal orientations of source-receiver pairs. If one medium is azimuthally anisotropic, however, the AVO response will also be a function of source-receiver azimuth. Rüger (1996) modified the AVO equations (4.1-4.2c) to include polar azimuthal anisotropy and gave reflection amplitudes between two weakly anisotropic (Thomsen, 1986) half spaces as:

$$A = \Delta Z_0/(2\overline{Z_0}) \tag{4.3a}$$

$$B = \frac{1}{2}\left(\frac{\Delta V_{p0}}{\bar{V}_{p0}} - \frac{\left(\frac{2\overline{V_{s0}}}{\overline{V_{p0}}}\right)^2 \Delta\mu_0}{\mu_0} + \Delta\delta \right) \tag{4.3b}$$

$$C = 1/2\left(\frac{\Delta V_{p0}}{\overline{V_{p0}}} + \Delta\epsilon\right) \tag{4.3c}$$

where Δδ and Δε are contrasts in Thomsen parameters δ and ε for HTI media and all quantities with a '*0*' subscript specifically indicate values for normal incidence ($\theta = 0$).

If the lower layer is an HTI medium, Equation 4.1 and specifically the AVO gradient term *B,* has been shown to have an elliptical form, but only at shorter offsets (θ < 35 degrees) (Rüger, 1996; Jenner, 2001). At longer offsets, the third term in Equation 4.1 becomes large and an elliptical form is not necessarily present. Therefore, limiting Equation 4.1 to these shorter offsets, the equation is rewritten as:

$$Rp(\theta) = A + B\sin^2(\theta) \tag{4.4a}$$

where the AVO gradient term B is now

$$B = \frac{1}{2}\left(\frac{\Delta V_{p0}}{\bar{V}_{p0}} - \frac{\left(\frac{2\overline{V_{s0}}}{\overline{V_{p0}}}\right)^2 \Delta\mu_0}{\mu_0} + \Delta\delta(\phi) \right) \tag{4.4b}$$

$$\Delta\delta(\phi) = \delta_1\cos^2(\phi - \phi_{rot}) + \delta_2\sin^2(\phi - \phi_{rot}) \tag{4.4c}$$

where ϕ is the azimuth and ϕ_{rot} is the azimuth of the major axis (rotation of the ellipse). The anisotropic term $\Delta\delta(\phi)$ has an elliptical form with δ_1 and δ_2 as the maximum and

minimum axes of the ellipse, respectively, and ϕ_{rot} is the azimuth describing the strike of the vertical fractures direction (Figure 4.1). Therefore, the fracture orientation is determined by fitting an ellipse to the AVO gradient term. Also, the ratio of the major and minor ellipse axes is used to estimate the relative fracture intensity (Montoya, 2002a), or a spatial variation in fracture intensity.

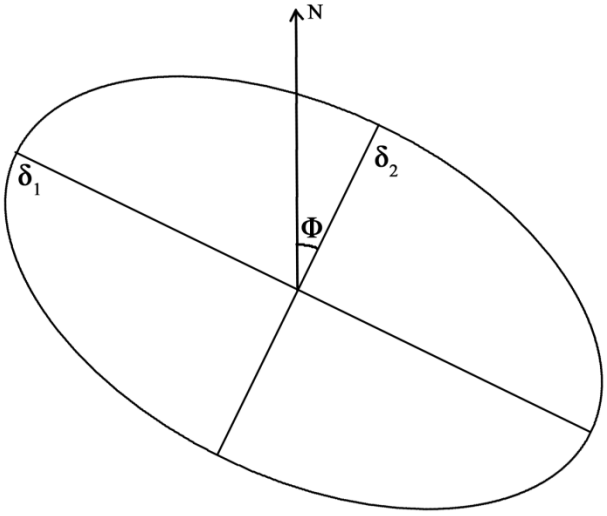

Figure 4.1 The anisotropic term $\delta(\phi)$ has an elliptical form with δ_1 and δ_2 as the maximum and minimum axes of the ellipse respectively, and $\Phi \equiv \phi_{rot}$ is the azimuth of the fracture orientation (modified from Montoya, 2002a).

ELLIPSE FITTING METHOD AND LIMITATIONS

The fitting of an ellipse to the gradient term derived from AVAZ data is useful to extract fracture orientation and relative fracture density, but the actual fitting itself is subject to some computational limitations. Shown here, only data subject to some constraints is fitted with an ellipse. The effect of these limitations is discussed in the next chapter when applied to the field seismic data.

An ellipse centered at the origin described in polar coordinates (r, ϕ) is:

$$r(\phi) = \sqrt{\frac{2a^2b^2}{(b^2 - a^2)\cos(2\phi - 2\phi_{rot}) + a^2 + b^2}} \tag{4.5}$$

where ϕ is the polar angle from the x-axis, a is the length of the major axis, b is the length of the minor axis, and ϕ_{rot} is the angle between the x-axis and the major axis (rotation of the ellipse).

The first limitation we can see is the minimum number of measurements (different source-receiver azimuths) required must be greater than 3, to solve for three unknowns ϕ_{rot}, a, b. Rearranging the equation (4.5) to solve for ϕ_{rot}:

$$\phi_{rot} = \frac{1}{2}[2\phi + \cos^{-1}(\frac{-2a^2b^2 + a^2r^2 + b^2r^2}{r^2(a^2 - b^2)})] \tag{4.6}$$

Therefore, given an r at a specific polar angle ϕ and a major and minor axis length a and b, the rotation of the ellipse was determined (although with one set of inputs, the rotation may be towards the major or minor axis due to the non-uniqueness of cos^{-1}). A limitation that may not be immediately apparent, but is inherent in graphing in polar coordinates, is that the values of r cannot change sign. Obviously, a negative r does not have much physical meaning, but if all of the r values are negative, the equation (4.6) shows that only r^2 is used and an ellipse can be fit. For data that change sign, as is possible when measuring B values from AVAZ as a function of azimuth, it is not possible to fit an ellipse. Only data that is either all positive or all negative may be amenable to fitting an ellipse. An immediate reaction would be to shift the data to either all positive or negative by adding a constant d or by taking the absolute value. This would be equivalent to increased contrasts across the interface to all positive or negative values at all

azimuths. The shift can easily be seen not to produce the same ϕ_{rot} if *r, a, b* are replaced by *r+d, a+d, b+d* due to the generation of cross-terms. However, it can be shown that multiplying all data by a constant *c* causes no change to ϕ_{rot} in the equation (4.6) by replacing *r, a, b* with *cr, ca, cb*. The constant *c* can be factored out of the denominator and numerator of the inverse cosine term and cancelled. This fact also confirms that all negative data can be used, because the multiplication of data by -1 is valid under these conditions. Unfortunately, multiplying by a constant does not help the problem of changing-sign data. Therefore, I conclude that for all practical purposes, fitting an ellipse to AVAZ results requires more than 3 points that are all of the same sign.

With these limitations in mind, the ellipse fitting method used in this study is an implementation of a least-squares fit method to the conic-equation of an ellipse described in work by Fitzgibbon (1999). It provides a fit to the major and minor axes and a rotation to the minor axis, which allows an axis ratio and orientation to be established for the characterization of fractures.

SUMMARY

This chapter demonstrated the theory and background of the amplitude varying with angle and azimuth (AVAZ) method and its application to the detection of horizontal transverse isotropy, specifically, fracture orientation and density. Ellipse fitting methods are integral to the interpretation of AVAZ results and their constraints are discussed in this chapter. From the methods described here, fracture orientation and relative variations in fracture density are estimated and the method's application to both field seismic data and modeled data was the basis for this project.

Chapter V: AVAZ Application to Seismic Data

SEISMIC DATA BACKGROUND

The 3-D seismic survey used in this work encompasses 14.3 square miles of the Anadarko Basin in Canadian County, Oklahoma. The survey area was rectangular in shape, spanning 2.7 miles E-W and 5.3 miles N-S. The survey was recorded with 3-component geophones, allowing for the measurement of both P-waves and converted P-S waves, although P-wave data is the primary source used here. Processed post-stack data and raw pre-stack data were provided, and both were used in this work. The pre-stack data were processed while preserving amplitudes, a necessary requirement of AVAZ analysis. This requirement restricted the full migration of the pre-stack data due to potential contamination of reflection amplitudes. Although others are investigating methods to avoid this (Zheng, 2011), it is not considered in this investigation. The acquisition configuration is shown in Figure 5.1, where the source and receiver grid are seen, as well as the resultant CMP fold.

SEISMIC DATA METHODOLOGY

To fully analyze the seismic data for AVAZ results, several processing and analysis steps were implemented using the Hampson Russell suite of analysis software. The outline is discussed here first, and the results are given in the next section. Firstly, the borehole well log was tied in two-way reflection time to the post-stack data to establish the depth of the Woodford in the surface seismic data. Second, the reflecting horizon was then interpreted in the post-stack data for the entire seismic survey area.

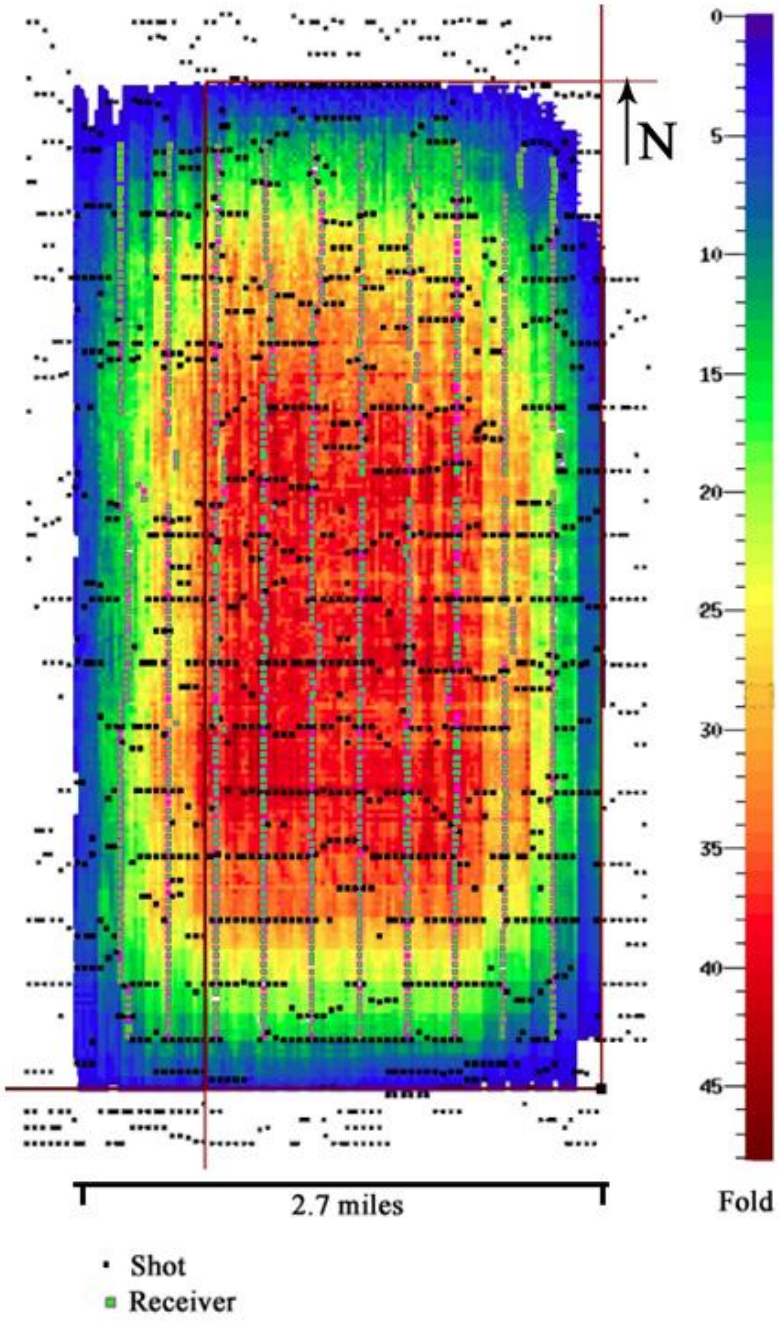

Figure 5.1 Acquisition layout of the seismic survey in Canadian County, Oklahoma. The 2.7 x 5.3 mile survey area is color-coded by CMP fold provided by the survey. The total number of shots used was 1,531 and receivers used was 1,101. Shot lines are oriented E-W while receiver lines are oriented N-S.

With this reflecting horizon defined, it was applied to the pre-stack data to allow for consistent picking of the Woodford reflection on the 3-D CMP gathers. Thirdly, the pre-stack data were divided into ten-degree azimuthal sectors, corrected for moveout to flatten the reflection horizons, and converted from offset gathers to angle gathers. Lastly, for each CMP, the AVO gradient *B* was estimated for each azimuthal sector, resulting in a measurement of *B* as a function of azimuth for each CMP gather with a sufficient number of traces.

From this work, a resultant set of *B* values as a function of azimuth was computed for the seismic survey. Each CMP then had an ellipse fit applied to the corresponding data (that satisfied constraints from Chapter IV) and an azimuthal direction and axis ratio was calculated. This dataset is the basis for maps and analysis discussed later in this chapter.

INTERMEDIATE RESULTS

Well to Seismic Tie

The tie between the surface seismic data to the well log within the seismic survey area was accomplished using eLog software in the Hampson Russell analysis package. From the seismic data, a statistical wavelet was extracted to generate the synthetic seismogram. Once extracted, the wavelet was convolved with the impedance log created from the P-wave and bulk density logs. The resulting seismogram is visually represented next to the seismic trace corresponding to the well location (Figure 5.2). From this, the synthetic seismogram was adjusted to match the seismic data until a high correlation was achieved (75%). Note the modest amplitude trough associated with the top of the

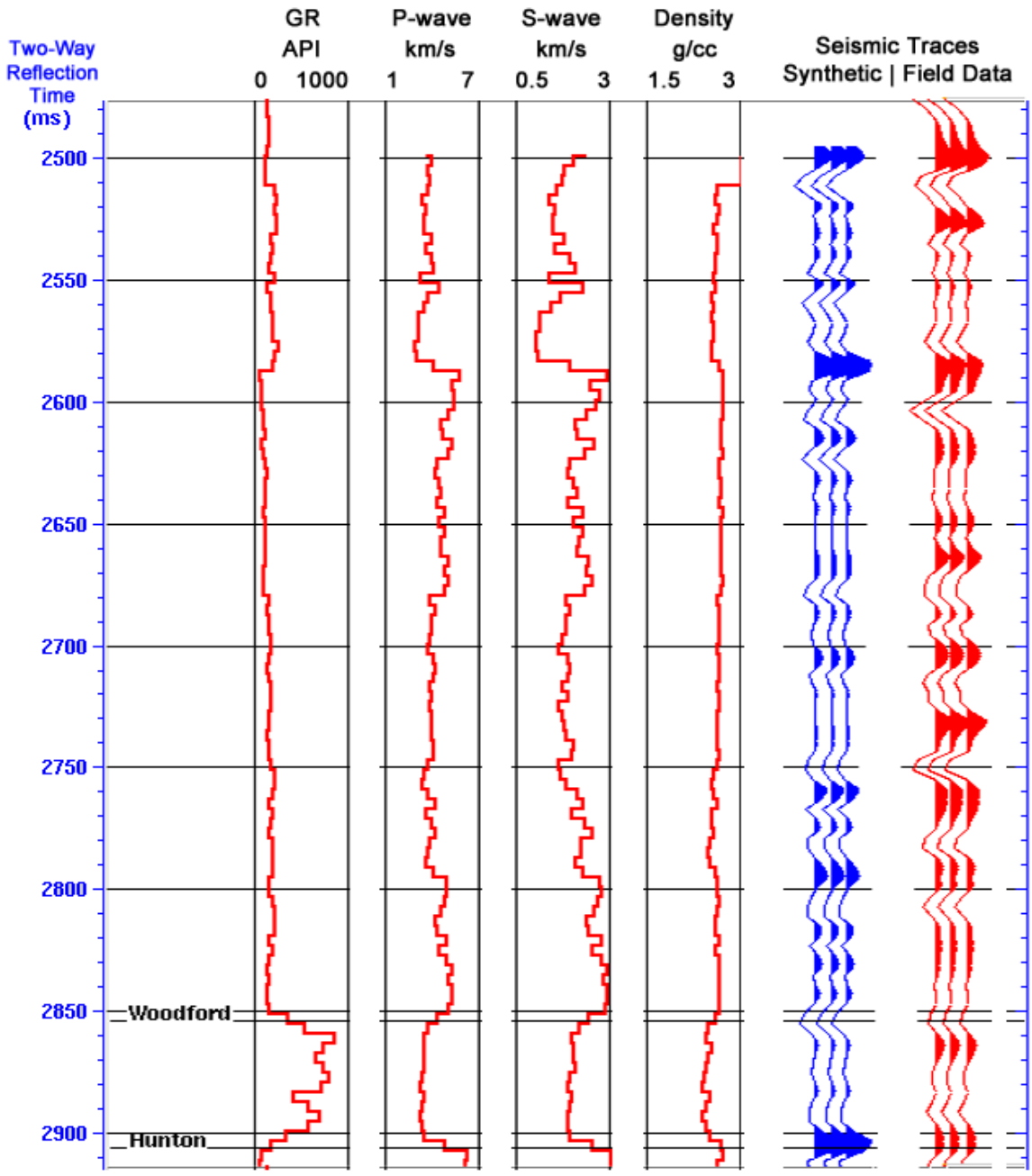

Figure 5.2 Correlation of the well log plotted in two-way reflection time to the seismic data using synthetic seismogram. From left to right: Gamma Ray, P-wave velocity, S-wave velocity, bulk density, synthetic seismogram (blue), extracted trace from data at specific inline and crossline (red). I use the top of the Woodford reflection for the analysis of the AVO gradient in the survey area.

Woodford reflection and the strong peak associated at the base of the Woodford on the synthetic seismogram, as the impedance contrast due to the change in P-wave velocity is more gradual at the top than the sharp contrast with the Hunton limestone at the base. The trough at the top is quite consistent on the synthetic and the real data; the large peak at the base is less of a contrast on the real data. While scaling may be the obvious difference, the wavelet is statistically extracted from the field data and may not generate an exact synthetic. Overall, the tie was correlated well giving a high degree of confidence that the horizon representing the top of the Woodford was known.

Horizon Interpretation

Once the horizons for the top and base of the Woodford Shale had been established at the well location from the well tie, it was then expanded for the entire seismic survey. This was done in the STRATA interpretation function as part of the Hampson Russell analysis package and was interpreted manually for every fifth inline and crossline. The horizon between these small intervals was automatically picked and then verified before continuing the analysis. Figure 5.3 shows the mapped horizon of the top of the Woodford Shale in the time domain. A clear NW-SE strike and SW dip is visible, consistent with regional geologic maps of the area. Over the 6 miles traversing NE-SW across the survey, the horizon dips approximately 200 ms (or 1590 ft). This is an average dip of 5 degrees SW. The interpreted horizon from the post-stack data was then used to interpret the pre-stack data at specific reflection horizons. Pre-stack data was used for analysis from this point onward.

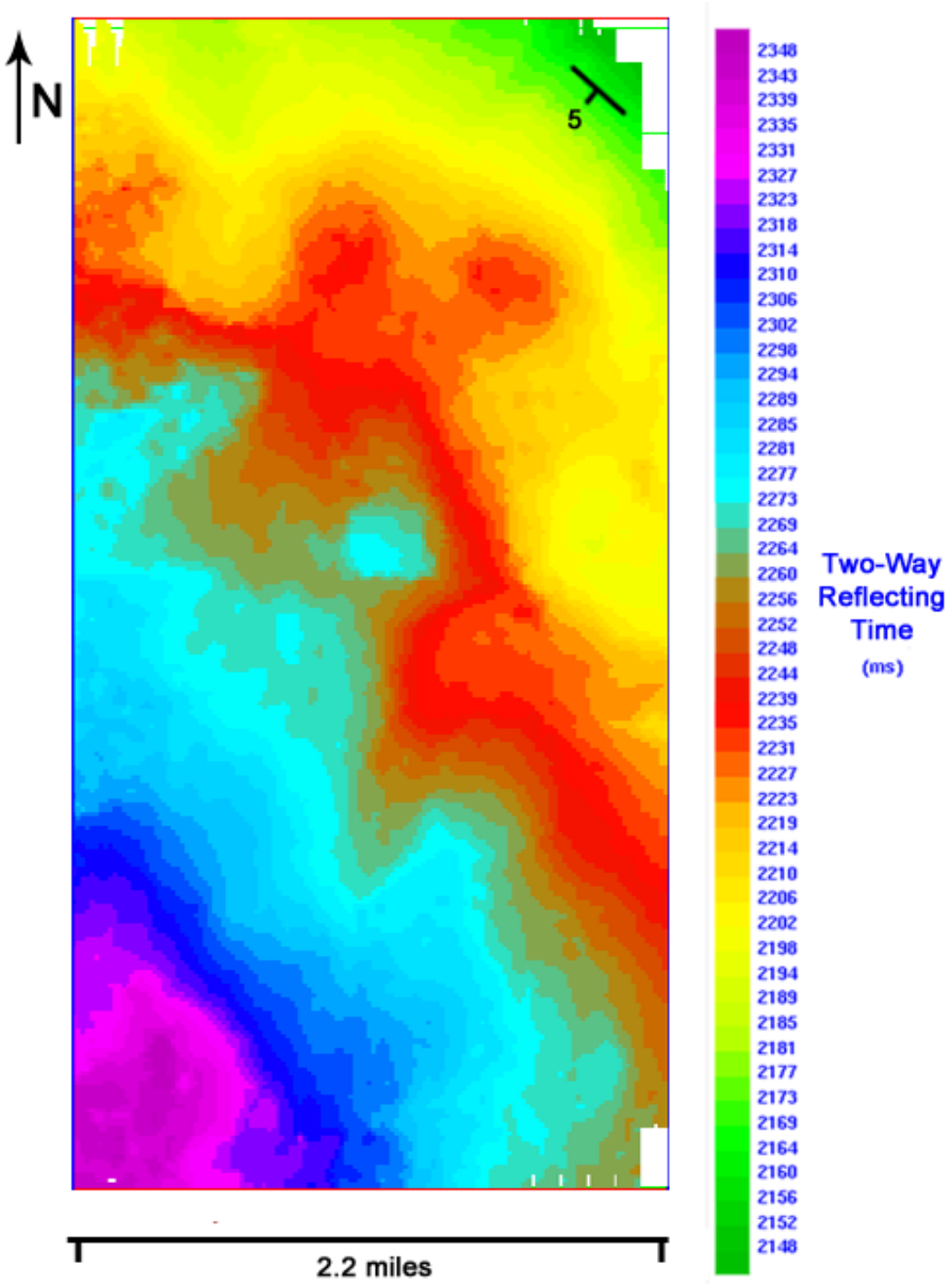

Figure 5.3 Display of the reflecting horizon representing the top of the Woodford Shale in the CMP stacked seismic data. A southwest dipping monoclinal trend is observed across the survey area. The average dip from NE to SW across the survey area is 5 degrees.

Sectoring the Pre-Stack CMP Data

To perform AVAZ analysis on the pre-stack data, it was gathered into 36 azimuthal sectors ranging in ten degree increments from 0-360 degrees. Each sector was paired with its complement (+180 degrees) sector. (Figure 5.4) This allowed all AVAZ analysis in each sector to ensure the azimuth between the source and receiver was limited to a defined range. The number of CMPs in each azimuthal sector varied due to source and receiver acquisition geometry, but each sector had sufficient numbers to analyze. A histogram of the total number of CMPs available in each azimuth is shown in Figure 5.5. A total of 730,000 CMP bins were used in the survey, with an average of 19,000 per azimuthal sector. Due to the rectangular shape of the survey, the bias towards source-receiver pairs having a north or south orientation (0 or 180 degrees, respectively) is clearly visible. Nonetheless, even at an azimuth of 90° (east-west), there was an average of 7,000 CMP positions available.

Conversion to Angle Gather and Correcting Moveout

Each of the CMP traces in the ten-degree azimuthal sectors were converted (through an application of the Hampson Russell analysis package) from an offset gather to an angle gather based on time-depth conversion from the borehole P-wave velocity log. This allowed all traces to be shown as depth vs. incidence angle. Also as part of the angle gather conversion, normal moveout correction was applied to flatten horizons. The angle of incidence for a constant offset trace decreases with depth, while the offset increases with depth for a constant angle trace (Figure 5.6). The need for the traces to be expressed as a function of angle is a requirement of AVAZ, in order to facilitate fitting it to the Shuey (1985) approximation equation $A + B \sin^2 \theta$. Visualizing the difference of synthetic seismic data before and after conversion to angle gathers and application of moveout correction is seen in Figure 5.7.

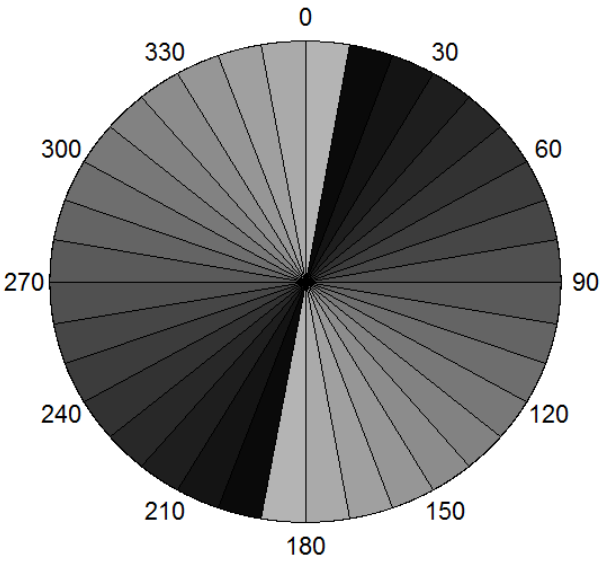

Figure 5.4 Visualization of azimuthal sectors used for AVAZ analysis. A total of 18 ten-degree azimuthal sectors and their corresponding sector complements (+180 degrees) were grouped and analyzed.

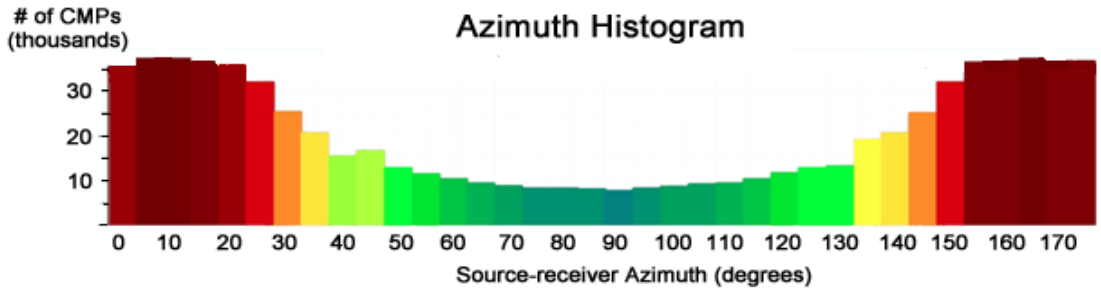

Figure 5.5 Histogram of number of CMPs available with each azimuthal sector between each source and receiver pair. Each column is a range of 5 degrees spanning from 0 to 180 degrees. With the rectangular shape of the survey covering a farther distance N-S, the influence shows in the higher number of CMPs with source-receiver azimuths near 0 (North) and 180 (South).

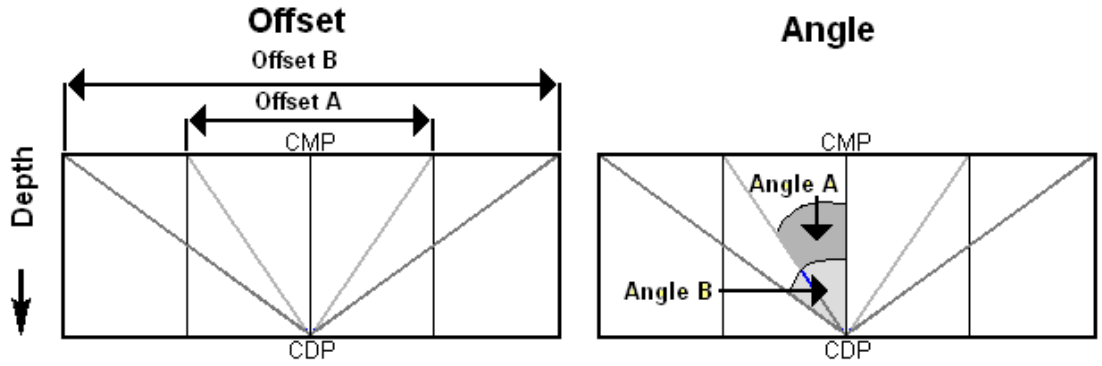

Figure 5.6 Visualization of conversion from offset gathers to angle gathers (modified from documentation in the Hampson Russell Assistant - Offset to Angle Theory).

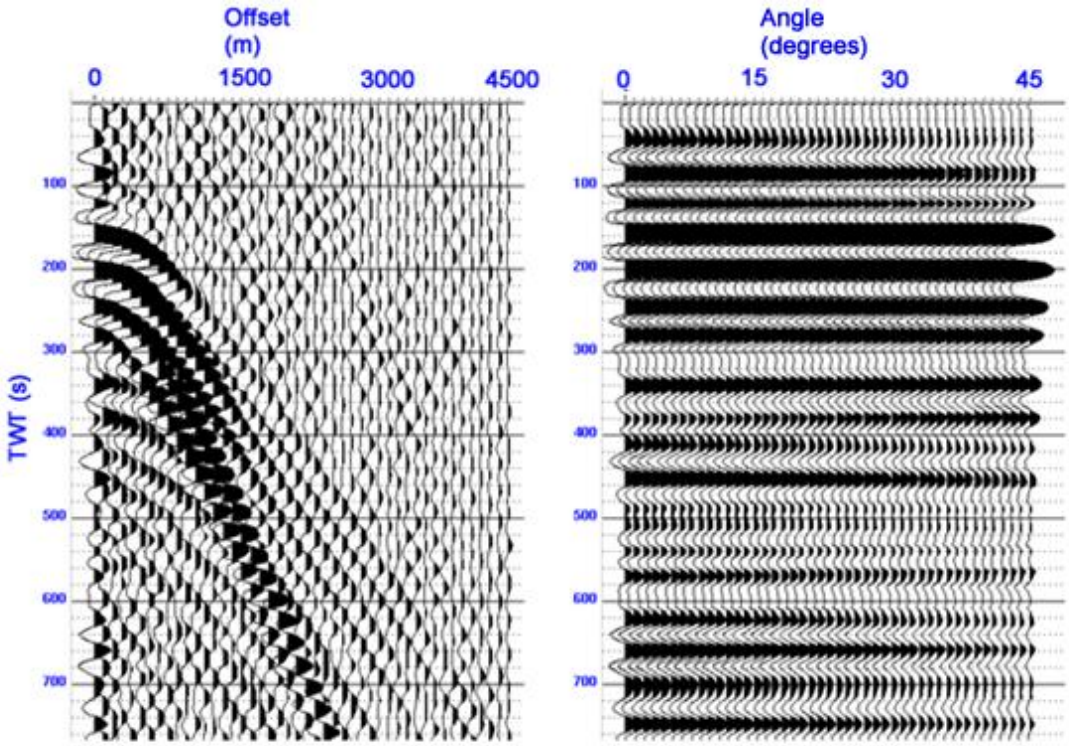

Figure 5.7 A visualization of seismic data before (left) and after (right) a conversion from offset to angle gather and a normal moveout correction has as applied. The moveout correction is based on a velocity model from the borehole log in the survey area.

Estimating the AVO Gradient

Once the azimuthal sectors of pre-stack data have been converted to angle gathers and then corrected for moveout, the horizons appear flat on a CMP gather of depth vs. offset for each range of incidence angle. From these data, the interpreted horizon for the top of the Woodford Shale (identified on the stacked data) was used to select the reflection amplitude as a function of incidence angle. Having the reflection amplitude as a function of incidence angle θ allows the fitting of this data with $\sin^2\theta$, as shown by Shuey's (1985) approximation $A + B\sin^2\theta$. This approximation allows for the fitting of the data to the parameters *A,* known as the intercept, and *B,* the AVO gradient. This method was repeated for each CMP gather in each azimuthal sector. The result was a dataset for each CMP (that had sufficient data) that contained its location and its AVO gradient term *B* for each azimuthal sector. Figure 5.8a-b shows a method of picking the reflection amplitudes along a horizon and then fitting the amplitudes to *A* and *B*.

AVAZ RESULTS

Ellipse Fitting

In Chapter IV, the inherent limitations of fitting ellipses to data were discussed, and any data that did not meet these limitations were disqualified for analysis. Specifically, any CMP gather that had fewer than three azimuthal measurements or AVO gradient (*B*) measurements that changed sign and contained both positive and negative values were discarded. For each CMP gather, an ellipse was fit to the AVO gradient data as a function of azimuth. To check the sensitivity of this method, a bootstrapping method was performed where an ellipse was fit to the same dataset with each individual point removed once.

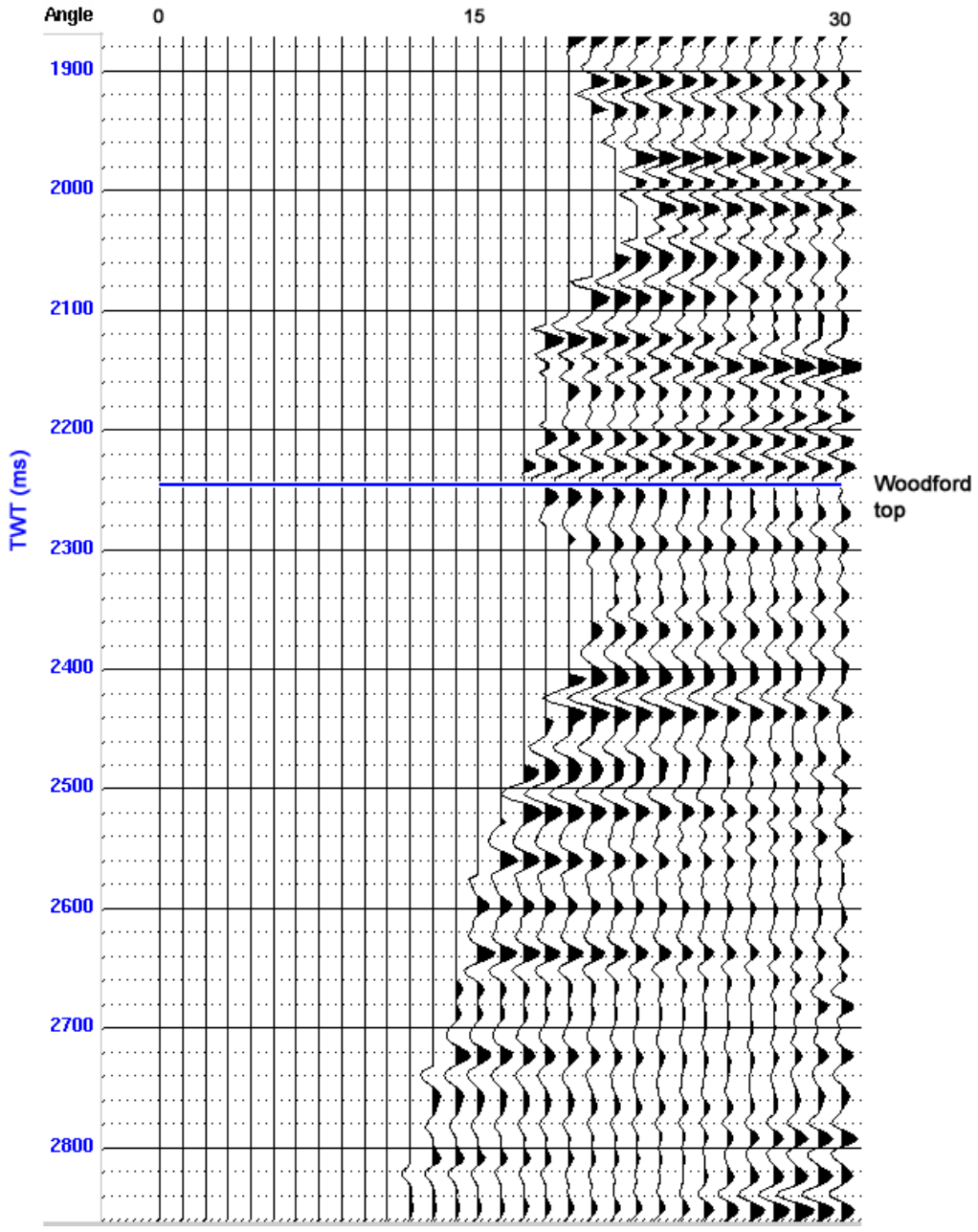

Figure 5.8a AVO Gradient analysis interpretation. Reflection amplitudes along the Woodford Shale horizon for a single CMP are shown as a function of offset angle (x-axis). Their fit to the Shuey (1985) approximation is shown in Figure 5.8b. Note that for this CMP and azimuthal sector, no near offsets (or small angles) were recorded.

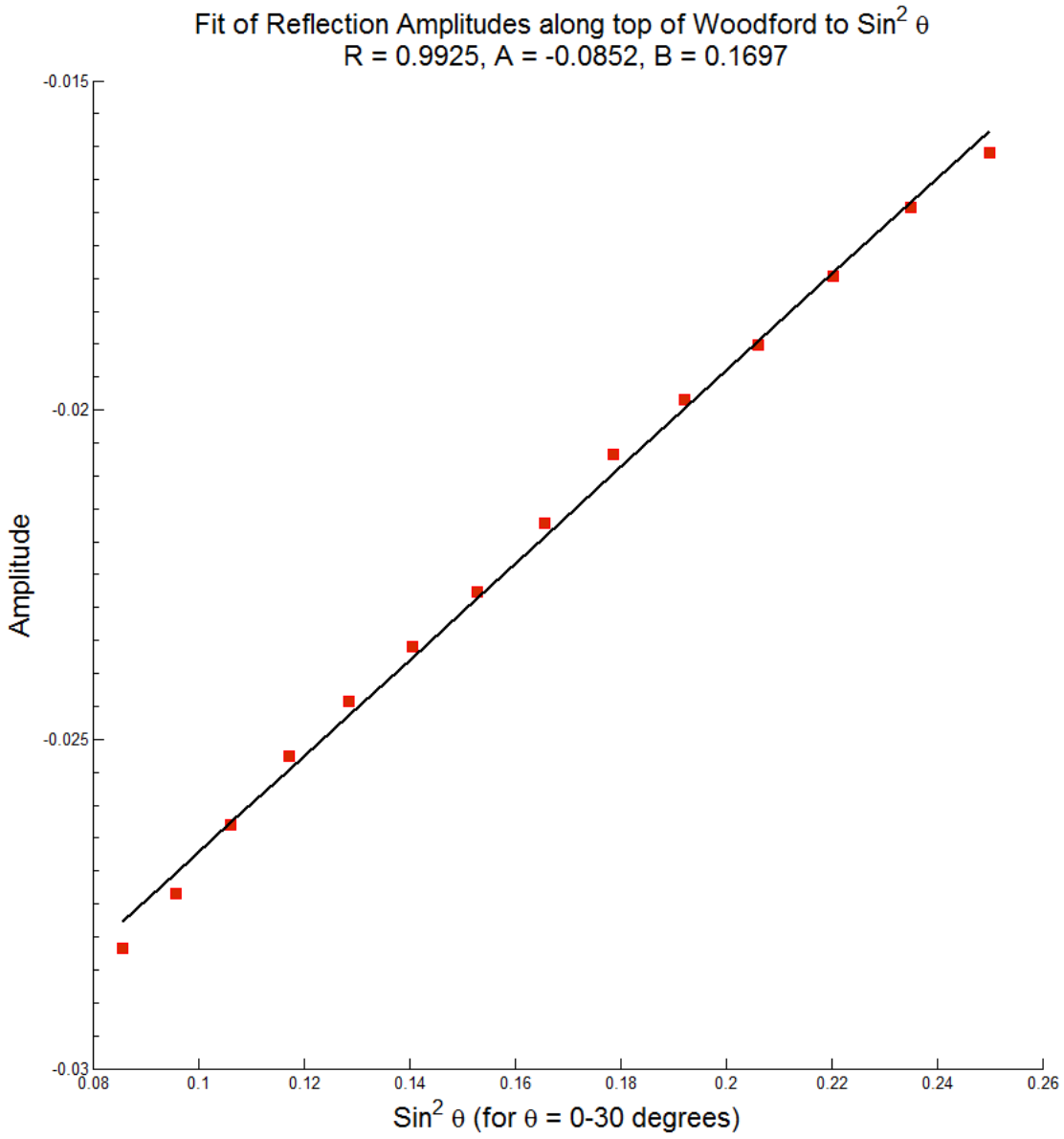

Figure 5.8b Corresponding reflection amplitudes from Figure 5.8a shown plotted as a function of $\sin^2\theta$. A least-squares fit line is shown and its axis intercept and slope are measured as the AVO terms *A* and *B*.

For the bootstrapping method, for example, an ellipse fit to five data points was performed by also fitting an ellipse to each subset of four data points and the residual error calculated. The subset (with one value omitted) with the least error was the best fit and the corresponding ellipse was selected for analysis. This bootstrapping method helped eliminate outliers that were skewing the estimation of ellipse parameters.

Fracture Orientation

To visualize the large amount of information from a regional map of fracture orientation and relative intensity, the data were broken down in several parts. From the results obtained in the ellipse fitting of all the appreciable CMP's, the dominant fracture direction (ellipse minor axis) of the entire region is shown as a rose diagram (Figure 5.9). The N65°E direction (and its S65°W counterpart) clearly stands out and possibly a smaller S70°E secondary set. Spatially, these fracture orientation estimates cover the majority of the seismic survey although the edges of the survey could not be fit to ellipses due to insufficient data at the boundaries. The map of the survey area with these orientation measurements is seen in Figure 5.10a. The dominant stress direction of the overburden has been shown to be west to east (Roche, personal communication, 2012), which agrees with the data shown here.

In Figure 5.10b, these fracture orientation estimates are overlain on the reflection horizon of the top of the Woodford (from Figure 5.3). Once superimposed on the structure, the fracture orientations are noticeably seen to follow major structural features and also align themselves with the strike of the layer. The structural map is integral to understanding the complicated nature of the fracture orientations in the region.

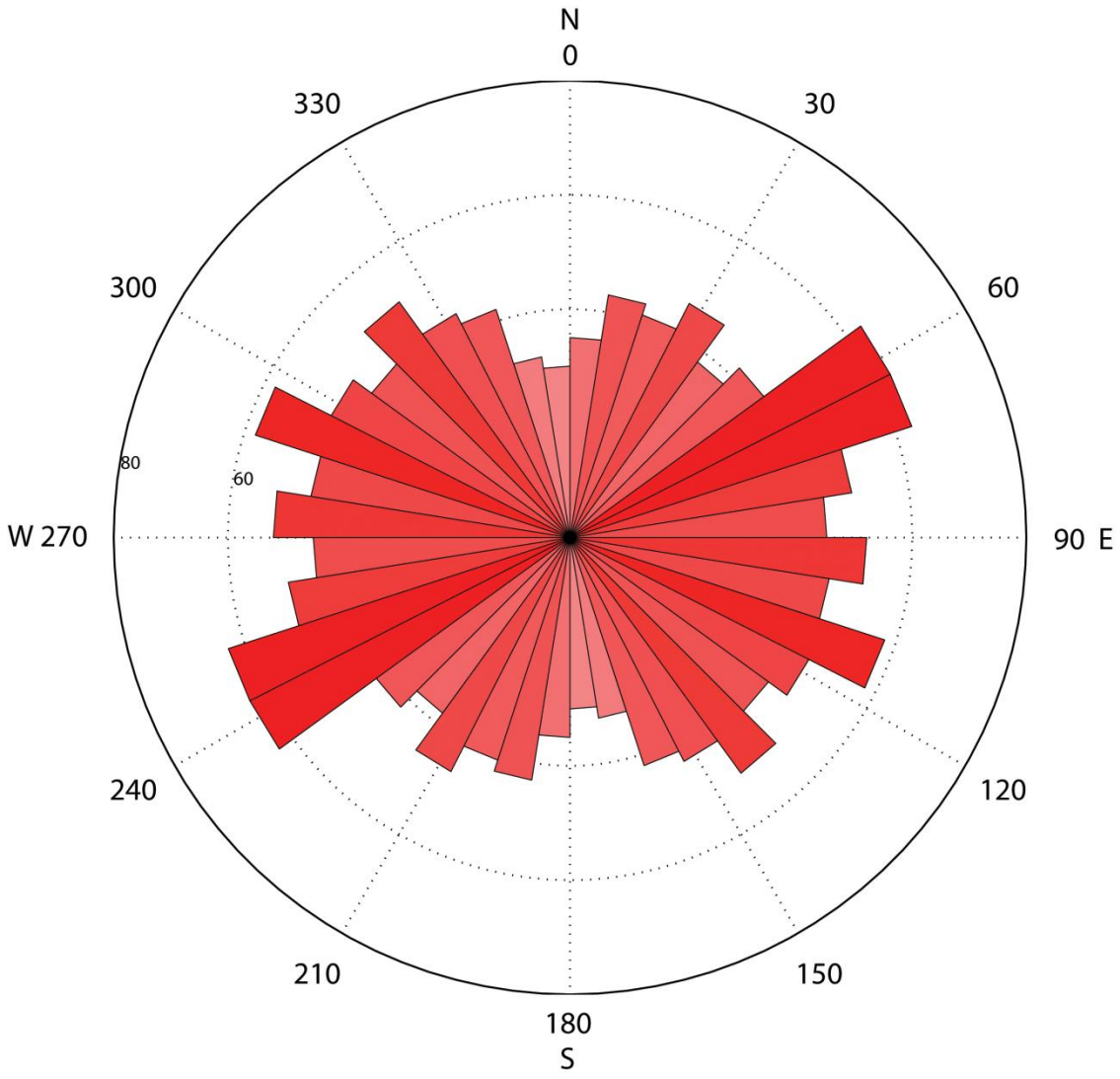

Figure 5.9 Rose diagram of the fracture orientation as a result of AVAZ analysis of all the CMP gathers of the Woodford Shale in Canadian County, Oklahoma. Two dominant dip directions are observed. However, the SW-NE direction appears to be the most dominant fracture direction, which is consistent with the overall dip orientation in the survey area. The color shading corresponds to the histogram count in each azimuthal direction.

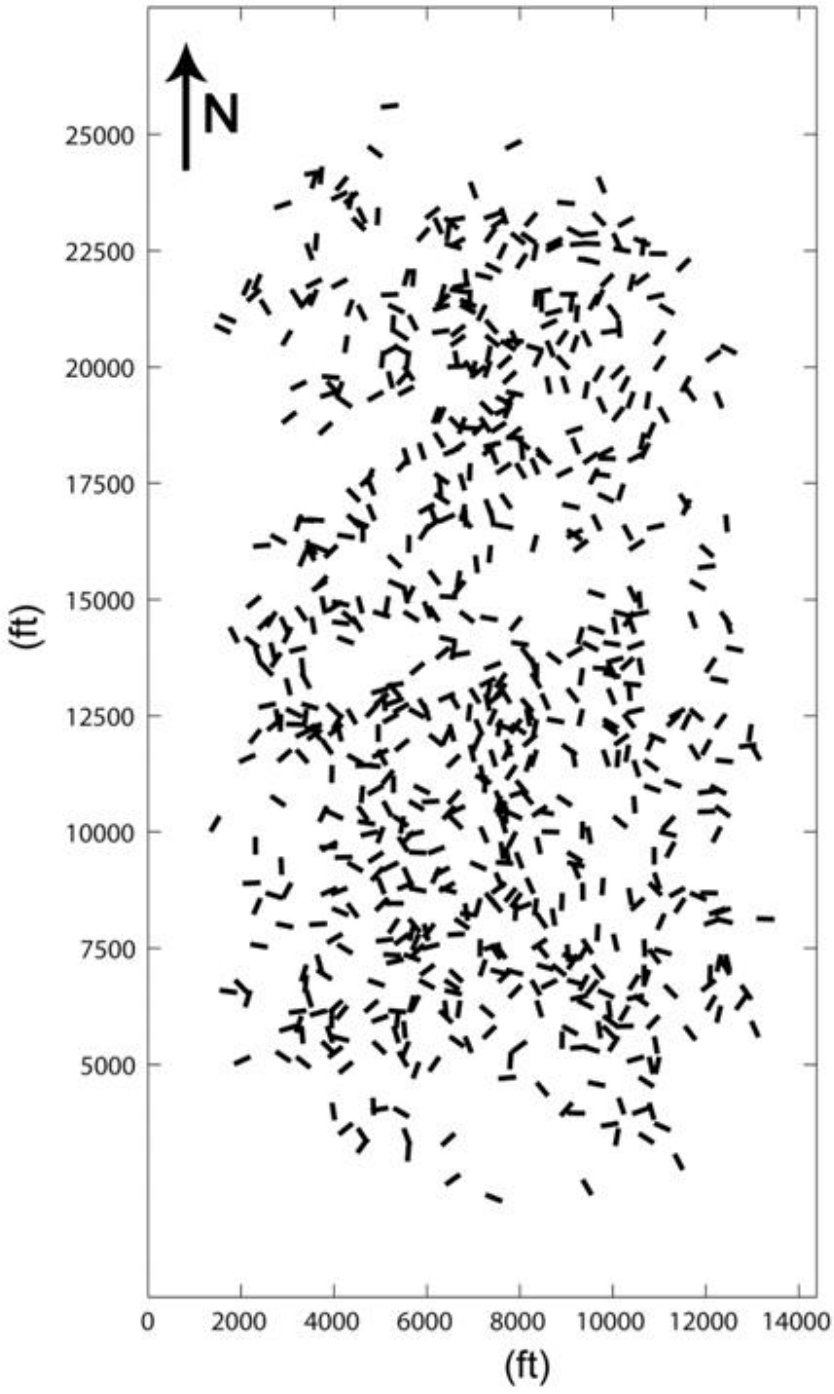

Figure 5.10a Map view of the fracture orientation measurements over the seismic survey from AVAZ analysis. The dominant direction is N65°E-S65°W (Figure 5.9). This can be compared to the structure map (5.10b).

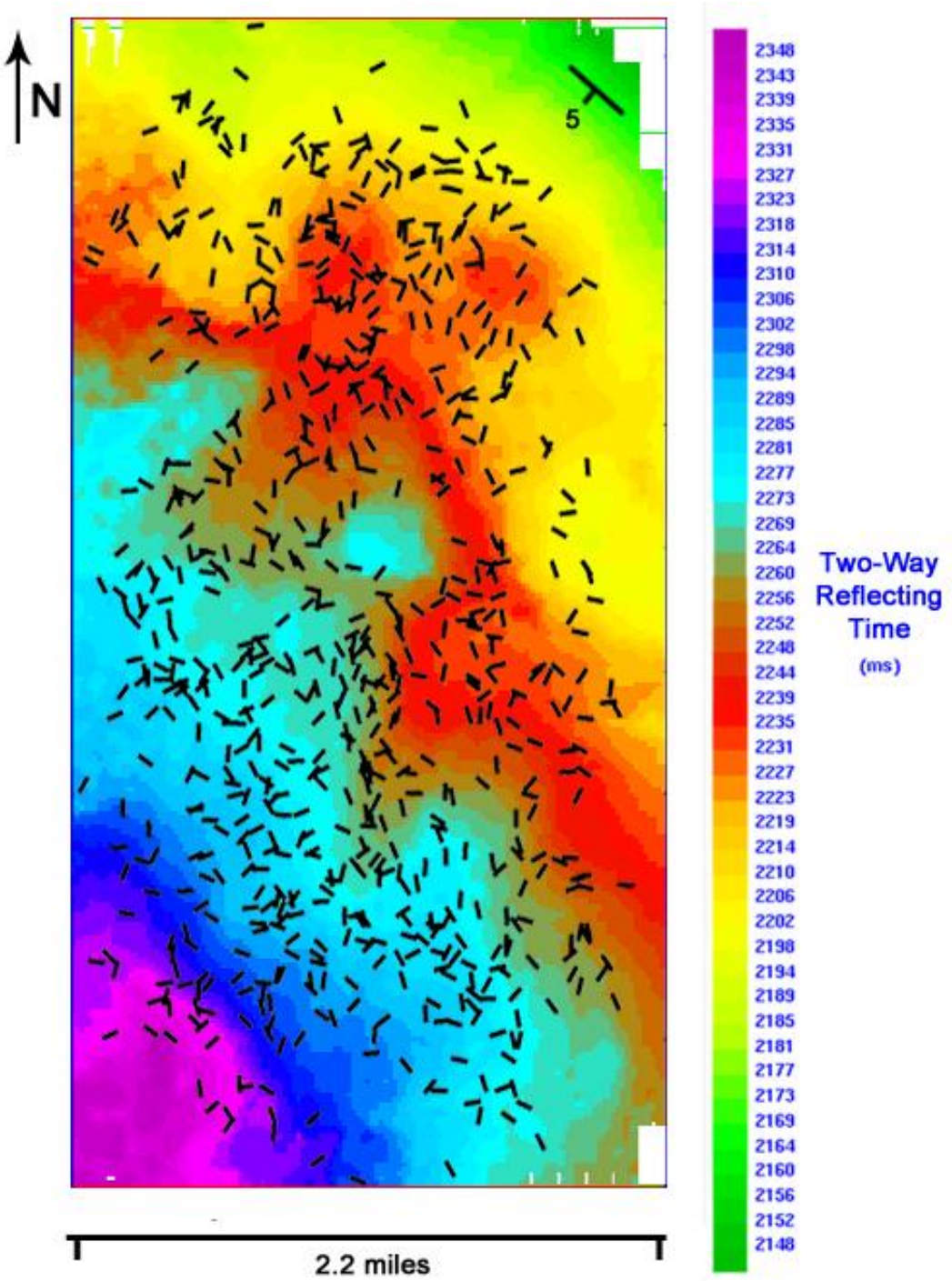

Figure 5.10b Map view of the fracture orientation measurements overlain on the reflection horizon of the Woodford shale (Figure 5.3). A dominant trend of fractures orienting along structural features is visible.

Fracture Intensity

The ratio of the major to minor axes of the ellipse fitted to AVAZ data is correlated to the level of fracture intensity. The more elongated the ellipse, the higher the ratio and the higher fracture intensity present there. Figure 5.11 shows a map view of the fracture intensity of the survey. The intensity does not seem to correlate as strongly with structural features as orientation does. However, a large portion of higher crack intensity surrounds the structural portion between 2220 and 2250 ms (shown in red in Figure 5.10b), and lower crack intensity does appear to have some connectivity around pockets of higher intensity.

"Higher" fracture intensity, in this sense, is a relative term; a quantitative fracture density cannot be extracted from these results alone (Rüger, 2002). Further work in this project using rock physics modeling seeks to address this problem and establish the connection between ellipse axis ratio and absolute crack density. The axis ratios in the field seismic data numerically range from 1 to 11 and their corresponding crack density values are addressed in Chapter VII.

SUMMARY

The methodology presented here, as well as the intermediate and final results, show the viability of describing fracture orientation and intensity using AVAZ for this seismic data. The visualization of the final results is seen in Figure 5.12. From a production perspective, the highest fracture intensity areas would be more exploitable and the orientation provides a direction, normal to which, to horizontally drill.

Key methods included in this chapter are 1) the tying of well data to post-stack seismic data to ensure the correct reflection was used; 2) the use of post-stack data to interpret the horizon of choice for AVAZ analysis; and 3) the use of pre-stack data that

has amplitudes preserved to ensure the AVO gradient *B* term is unaffected. Finally, while AVAZ analysis does establish the areas for highest fracture intensity, it still only demonstrates a relative difference and a main goal of this project is to quantify the fracture density. The methods to complete this begin in the next chapter.

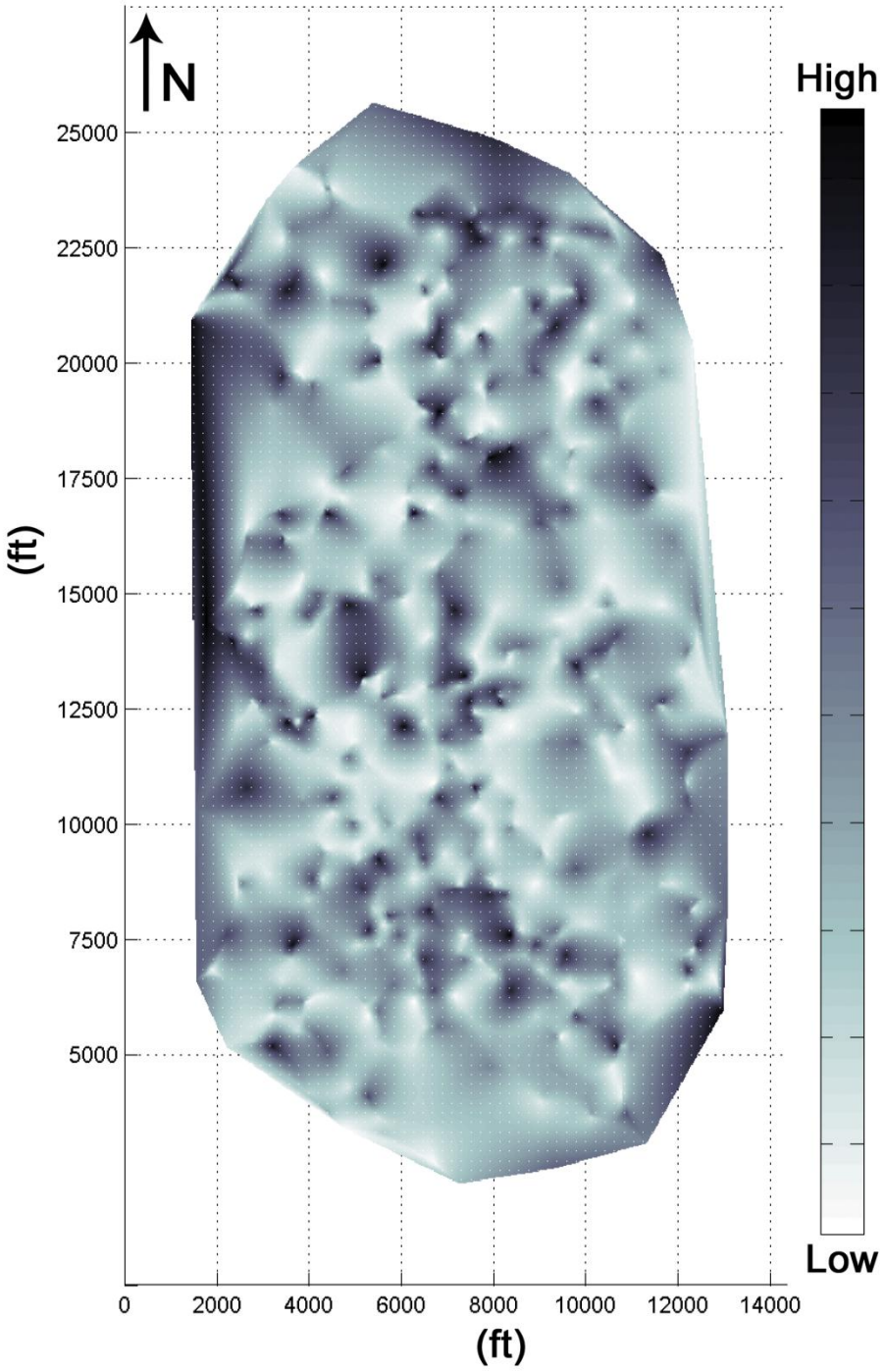

Figure 5.11 Map view of the fracture intensity measurements over the entire seismic survey from AVAZ analysis. These measurements only give a relative sense of the fracture intensity and further work is needed to actually quantify the fracture density.

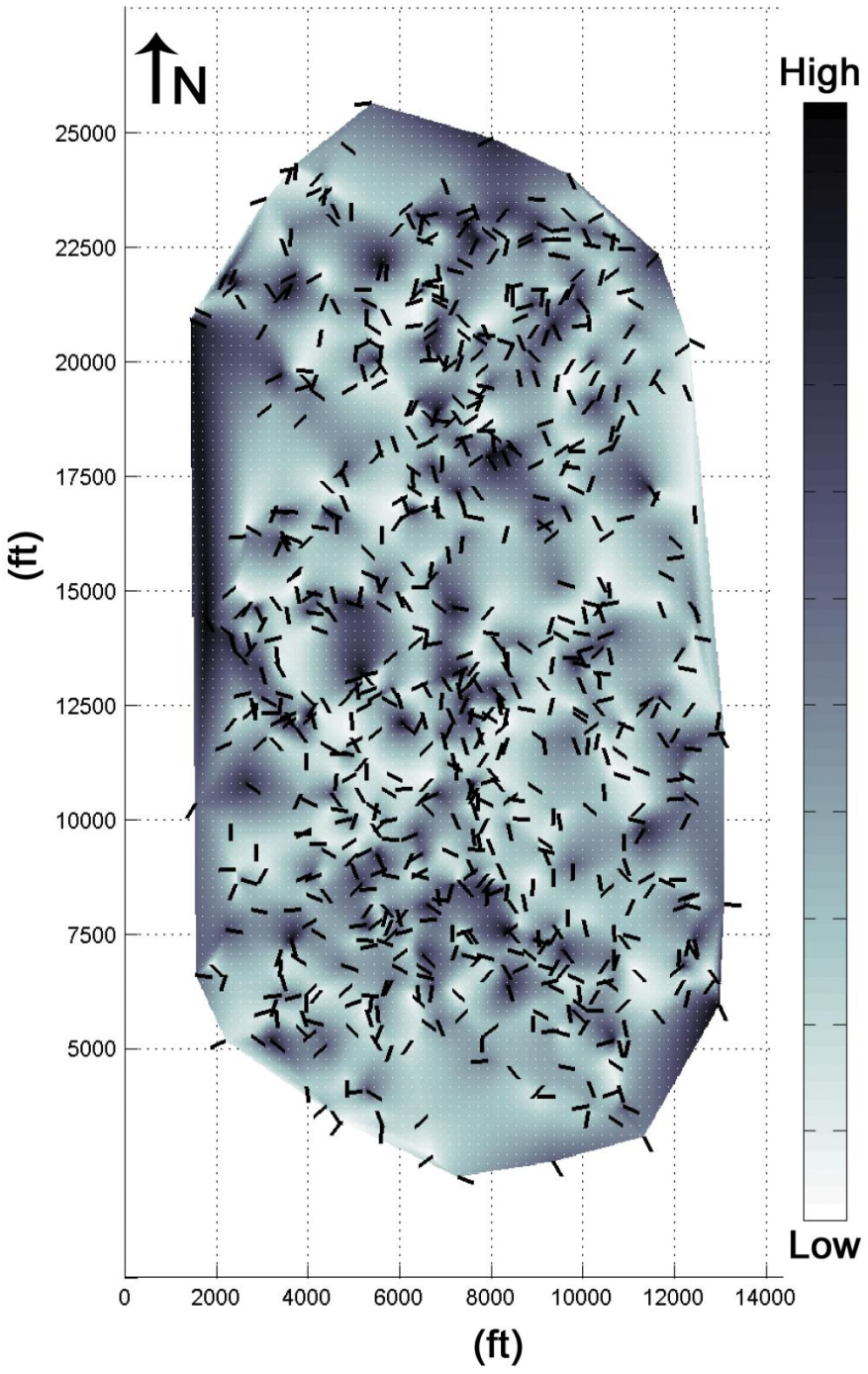

Figure 5.12 Map view of the fracture intensity and orientation measurements over the entire seismic survey from AVAZ analysis. This is a combination of Figures 5.10a and 5.11.

Chapter VI: Rock Physics Modeling

INTRODUCTION

To quantify the relative fracture density seen in Chapter V, an understanding of the effect of absolute fracture density on AVAZ results was investigated. With a rock physics model that takes fracture density as an input and emulates the Woodford Shale lithology and rock properties, a connection was established between an absolute fracture density and the ellipse axis ratio determined by AVAZ analysis.

Four main elements comprise the rock physics modeling in this study. First, an estimation of the Woodford Shale mineral composition was made based on interpretation from the neutron-induced elemental gamma ray spectroscopy mineralogical borehole logs. Second, from this composition, bulk rock stiffnesses with porosity were estimated in the context of Hashin-Shtrikman-Walpole bounds (Berryman, 1995). Third, penny-shaped cracks were introduced to the model using methods by Hudson (1980). Lastly, fluid saturation was added to the model using the methods of Brown and Korringa (1975). The workflow used here is shown in Figure 6.1. Altogether, this procedure provided a model of a porous, cracked, fluid-saturated rock analogous to the Woodford Shale. This became the basis for our investigation into fracture density and its effect on AVO gradient. Previous studies have inverted sonic and dipole sonic log data for the stiffness tensor using effective medium theory (Bayuk et al., 2008), but the model presented here attempts to build upwards.

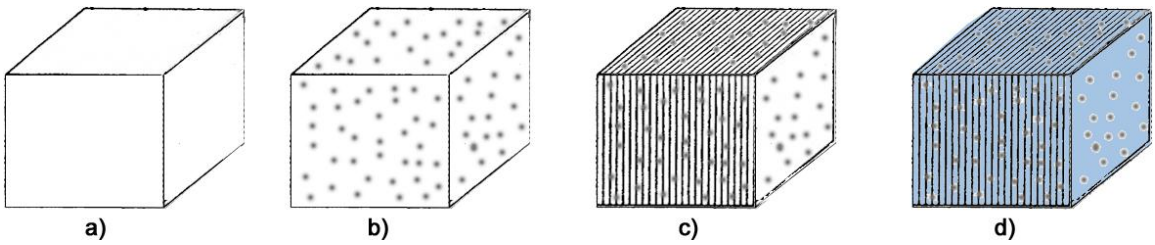

Figure 6.1 Visualization of rock physics modeling workflow: a) an isotropic block created from neutron-induced elemental gamma ray spectroscopy mineralogical logs, b) the introduction of porosity using Hashin-Shtrikman-Walpole bounds, c) the addition of cracks using the Hudson cracked media model, and d) fluid saturation using the methods of Brown and Korringa (1975).

COMPOSITE ESTIMATE

Mineralogy

To create the initial isotropic block in the rock physics modeling workflow, an investigation was performed into the mineralogical content of the Woodford Shale. The neutron-induced elemental gamma ray spectroscopy borehole well logs contained logs relating to mineralogy in five distinct groups: calcite, quartz, clay, pyrite, and kerogen. Figure 3.2 shows the mineralogy for the Woodford Shale and the surrounding limestones above and below. Measurements from the borehole log were taken every six inches and describe the fractions of these five minerals. Table 6.1 shows the average values over the formation. Note that the Woodford "Shale" is dominated by quartz (53.2%) and then clay minerals (33.8%). Nearly 6% kerogen content is also recognized. Very little (<2%) calcite is recognized.

Porosity

From the approximate mineralogies given below, combined with the water saturation log and bulk density log ρ_b, we can make a preliminary estimate of the porosity (ϕ) of the Woodford Shale for each log-depth value of density (Equation 6.1). Volumetrically averaging mineral densities gives ρ_m and assuming the fluid density ρ_f is a mixture of water and gas governed by the water saturation log, the porosity was calculated. Table 6.2 shows the data used. Once the isotropic mineralogy and porosity are calculated, the porosity-corrected K and μ values of the block was established using Hashin-Shtrikman-Walpole bounds.

$$\rho_b = (1 - \phi)\rho_m + \phi\rho_f \tag{6.1}$$

	Lower Mississippian limestone	Woodford Shale	Upper Hunton Limestone
Calcite	33.2%	1.8%	80.4%
Clay	14.6%	33.8%	6.6%
Pyrite	1.5%	5.3%	0.8%
Quartz	50.5%	53.2%	12.1%
Kerogen	0.2%	5.9%	0.0%

Table 6.1 Average mineralogical values for the lower Mississippian limestone, Woodford Shale, and upper Hunton Limestone.

	Bulk Modulus (GPA)	Shear Modulus (GPA)	Density (g/cm^3)
Calcite	77	32	2.75
Clay	21	7	2.60
Quartz	37	44	2.65
Pyrite	143	121	4.87
Kerogen	2.9	2.7	1.30
Gas	0.07	0	0.20
Water	2.6	0	1.05

Table 6.2 Material data used for composition estimates (Mavko et al., 2009).

HASHIN-SHTRIKMAN-WALPOLE BOUNDS

From the previous section, an estimation was made of the mineral composition with corresponding isotropic bulk modulus and shear modulus as a function of depth. To correct these moduli for the presence of porosity, the Hashin-Shtrikman-Walpole bounds (Berryman, 1995) were used to estimate the bounds of K and μ as a function of porosity for each measurement. The upper (HSW+) and lower (HSW-) bounds of K and μ are calculated (Equations 6.2a-e):

$$\mu^{HSW+} = \left[\frac{\phi}{\mu_f + X} + \sum_{k=1}^{M} \frac{(1-\phi)f_k}{\mu_k + X}\right]^{-1} - X \tag{6.2a}$$

$$X = \frac{\mu_{max}}{6}\left(\frac{9K_{max} + 8\mu_{max}}{K_{max} + 2\mu_{max}}\right) \tag{6.2b}$$

$$\mu^{HSW-} = \frac{\mu_{min}}{6}\left(\frac{9K_{min} + 8\mu_{min}}{K_{min} + 2\mu_{min}}\right) \tag{6.2c}$$

$$K^{HSW+} = \left[\frac{\phi}{K_f + \frac{4}{3}\mu_{max}} + \sum_{k=1}^{M} \frac{(1-\phi)f_k}{K_k + \frac{4}{3}\mu_{max}}\right]^{-1} - \frac{4}{3}\mu_{max} \tag{6.2d}$$

$$K^{HSW-} = \left[\frac{\phi}{K_f} + \sum_{k=1}^{M} \frac{(1-\phi)f_k}{K_k}\right]^{-1} - \frac{4}{3}\mu_{min} \tag{6.2e}$$

where M is the number of constituents, f_k is the constituent's fractional percentage of the medium, μ_f and K_f are the moduli of the fluid, μ_k and K_k are the moduli of a constituent, and μ_{max}, K_{max} and μ_{min}, K_{min} are the maximum and minimum moduli, respectively, of all constituents. These upper and lower bounds predict the range of effective elastic moduli of a mixture of grains and pores. In general, to specify these effective moduli,

three properties are needed: the volume fractions of the various phases, the elastic moduli of the various phases, and a geometric consideration of how the phases are arranged relative to each other (Mavko et al., 2009). Without specifying the geometric relationship between constituents, these bounds are shown to have the narrowest possible range (Mavko et al., 2009). The application of these bounds to the isotropic mineralogical block and a dry pore space allows the modeling of a porous block (step 2 in the rock physics workflow). The reasons for adding an empty pore space vs. adding the fluids initially is discussed in the section regarding fluid saturation later in this chapter.

The upper and lower bounds of the moduli were calculated for a mineralogical fraction (from our composite estimate) as a function of porosity. The calculated porosity (from Equation 6.1) was used to determine effective moduli as the average of the two bounds at that specific porosity (Figure 6.2). Once the effective moduli K and μ were obtained, the rock physics model described an isotropic block with porosity introduced. To further characterize the Woodford Shale, the next step involved the addition of vertical fractures using the Hudson cracked media model.

HUDSON CRACKED MEDIA MODEL

The Hudson cracked media model introduces thin, penny-shaped ellipsoidal cracks into an isotropic medium (Hudson, 1980). An effective stiffness tensor C_{ij}^{eff} was calculated from the isotropic background moduli C_{ij}^{0} corrected by C_{ij}^{1} (shown below in Equations 6.3a-f). A consideration when using the Hudson cracked media model assumes the seismic wavelength should be much larger than the scale length of the penny-shaped cracks. Further, the cracks are isolated and do not interact with one another. With a given

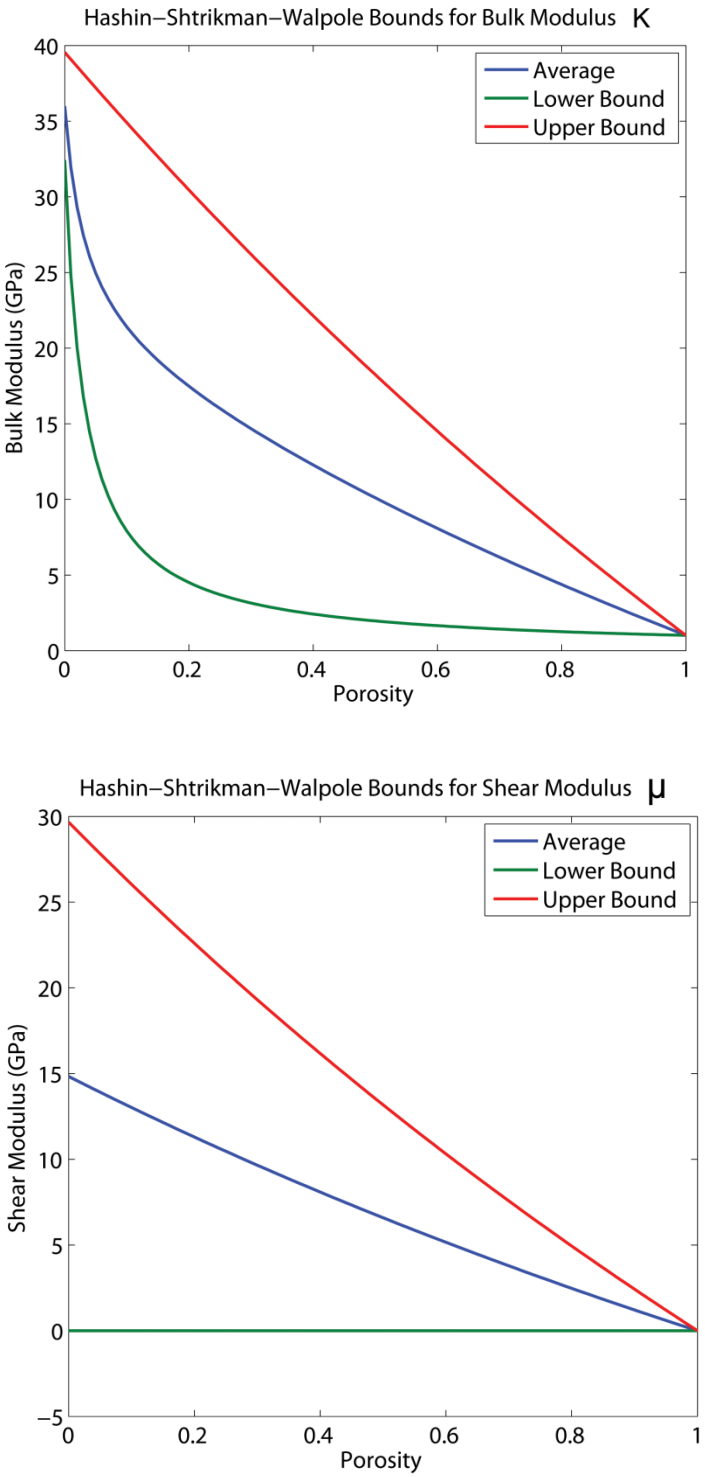

Figure 6.2 Hashin-Shtrikman-Walpole bounds for K (top) and μ (bottom). The average of the bounds at a calculated porosity was used as an effective modulus.

crack density ϵ and aspect ratio α, Hudson limits the crack porosity (Equation 6.4) to be consistent with non-interaction between cracks. Aspect ratio in this theory is defined as the ratio of the major and minor radii of the penny-shaped cracks. This crack porosity limitation comes from the idea that the larger the crack density, the more inclusions in the rock, and therefore a large enough crack density will cause the fractures to completely interact and the rock structure will fail. The Hudson model returns a modified stiffness tensor C_{ij}^{eff}. For this model, we assume the cracks to have small aspect ratios, which is another assumption of Hudson's method. In this case, we use α = 0.01.

$$C_{ij}^{eff} = C_{ij}^{0} + C_{ij}^{1} \tag{6.3a}$$

$$C_{11}^{1} = -\frac{\lambda^2}{\mu}\epsilon U_3 \tag{6.3b}$$

$$C_{13}^{1} = -\frac{\lambda(\lambda+2\mu)}{\mu}\epsilon U_3 \tag{6.3c}$$

$$C_{33}^{1} = -\frac{(\lambda+2\mu)^2}{\mu}\epsilon U_3 \tag{6.3d}$$

$$C_{44}^{1} = -\mu\epsilon U_1 \tag{6.3e}$$

$$C_{66}^{1} = 0 \tag{6.3f}$$

In this instance of dry cracks (saturation was modeled later), U_1 and U_3 are given as:

$$U_1 = \frac{16(\lambda+2\mu)}{3(3\lambda+4\mu)} \tag{6.3g}$$

$$U_3 = \frac{4(\lambda+2\mu)}{(3(\lambda+\mu))} \tag{6.3h}$$

The limitation of the relationship between crack density, crack porosity, and aspect ratio is:

$$\epsilon = \frac{3\phi^{crack}}{4\pi\alpha} \leq 0.1 \tag{6.4}$$

The inclusion of fractures into the porous, isotropic rock from previous steps now completes step 3 of the rock physics modeling workflow. It should be noted that the porosity is not in hydraulic communication. Fluid cannot move from pore to pore, fracture to fracture, or pore to fracture. To finish the modeling of the Woodford Shale, fluid saturation methods by Brown and Korringa (1975) will be applied.

BROWN AND KORRINGA FLUID SATURATION

The Brown and Korringa (1975) method for fluid saturation was used to introduce fluids into this model because of its application to anisotropic rock. Another consideration for its use comes from a limitation of Hudson's cracked media model. Hudson's method assumes cracks and pores are isolated with respect to fluid flow; therefore, pore pressures are unequilibrated and adiabatic. Hudson's model is appropriate to describe high-frequency laboratory conditions (Mavko et al., 2009). For low-frequency situations, however, the previous steps were used with a dry pore and crack space and then were saturated with Brown and Korringa's (1975) method.

After this model incorporated the cracks from the Hudson model, the material was still considered 'dry'. To incorporate fluids, the Brown and Korringa fluid saturation method was used, which takes the original compliance tensor, rock moduli, porosity, and the bulk modulus of the fluid as input. From this a corrected stiffness tensor was given:

$$s_{ijkl}^{sat} = s_{ijkl}^{dry} - \frac{\left(s_{ijaa}^{dry} - s_{ijaa}^{0}\right)\left(s_{bbkl}^{dry} - s_{bbkl}^{0}\right)}{\left(s_{ccdd}^{dry} - s_{ccdd}^{0}\right) + \phi(\beta_{fl} - \beta_0)} \tag{6.5}$$

where s_{ijkl}^{dry} is the effective elastic compliance tensor element of dry rock, s_{ijkl}^{sat} is the effective elastic compliance element of rock saturated with pore fluid, s_{ijkl}^{0} is the effective elastic compliance element of the solid mineral, β_{fl} is the fluid compressibility ($1/K_{fl}$), β_0 is the mineral compressibility ($s_{\alpha\alpha\gamma\gamma}^{0} = 1/K_0$), and ϕ is the porosity.

The difference between using the Brown and Korringa method to saturate fluids *after* using high-frequency models (such as Hudson's) and including the fluids from the start with the addition of pore space using Hashin-Shtrikman-Walpole bounds was significant. Because the Hudson (1980) model is considered high-frequency, its results more accurately predict laboratory data (where fluid equilibration is considered instantaneous). In a lower-frequency environment outside of the laboratory where fluid equilibration is part of the consideration, the Hudson model needs to be applied before fluid saturation to best fit the field data. Figure 6.3 shows the same calculation for the stiffness tensor element C_{33} using a fluid-saturated high-frequency model and a low-frequency model that was saturated as a final step. The scattered data shows values of C_{33} from the borehole log data and clearly shows an advantage to saturating the rock physics model after applying high-frequency models.

After applying all steps of the rock physics modeling workflow, the resulting final stiffness tensors (each for a specific crack density) represent the Woodford Shale corrected for porosity, cracks, and fluid saturation. It represents an HTI medium with natural fractures at a specific crack density and aspect ratio, a specific lithology, and was the basis for the synthetic seismic data generated and analytic analysis performed (these

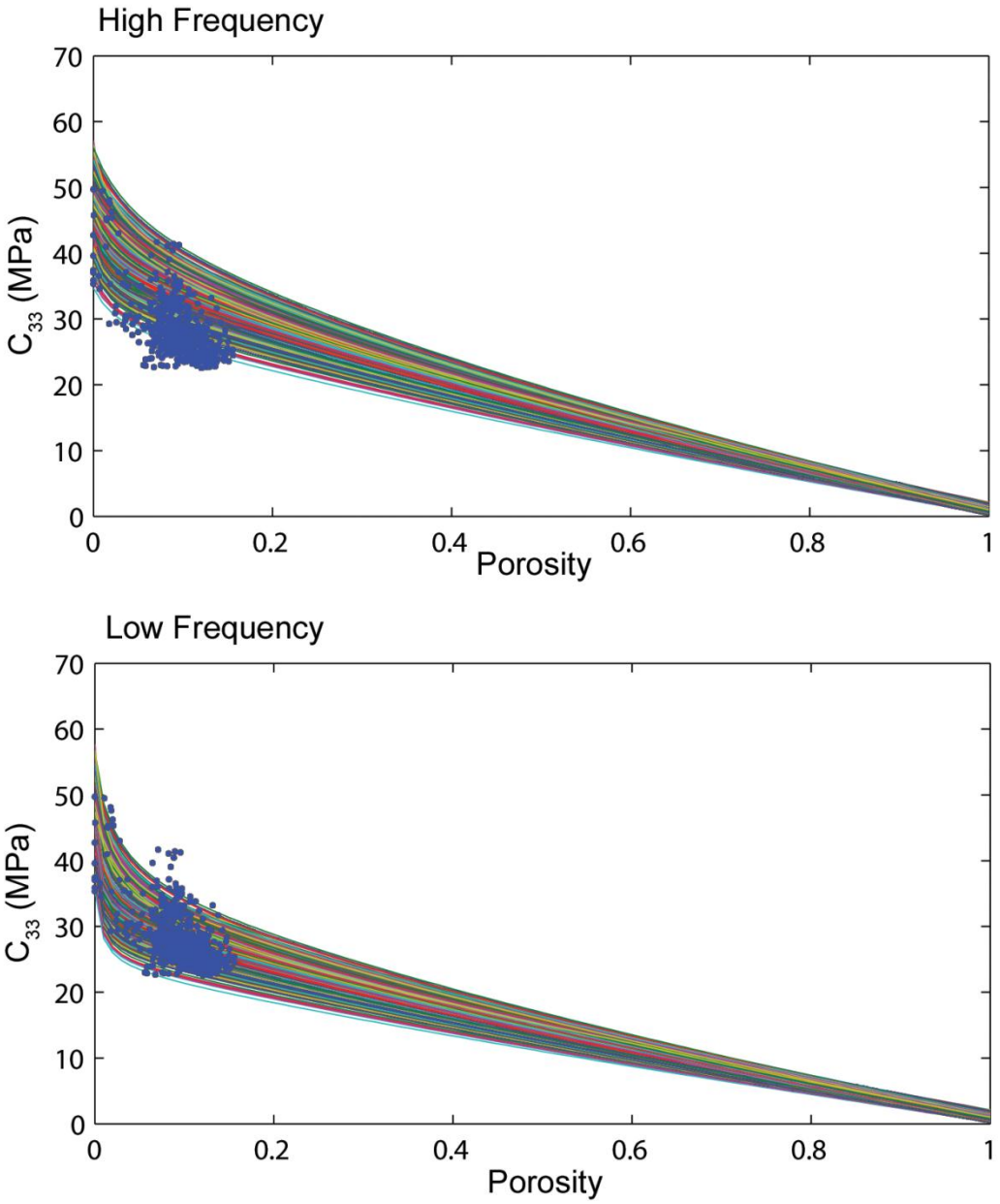

Figure 6.3 Estimation of stiffness tensor element C_{33} for high frequency and low frequency models. The high frequency calculations started with a fluid saturated isotropic rock before Hudson's model was introduced (top). The low frequency calculations had fluid saturation performed as the last step (bottom). The differently colored lines represent different compositions in the Woodford. Note the improved fit of the borehole data (scatter plot in blue) with the low-frequency workflow.

results are discussed in Chapter VII). The overlying layer, the Mississippian limestone, was modeled as an isotropic medium with stiffness tensor determined by the borehole log measurements of P-wave and S-wave velocity.

SUMMARY

The rock physics modeling in this chapter was composed of four main parts: the creation of an isotropic block from borehole mineralogical logs, the introduction of porosity and effective moduli using Hashin-Shtrikman-Walpole (Berryman, 1995) bounds, the addition of cracks to the model using methods of Hudson (1980), and finally fluid saturation using methods of Brown and Korringa (1975).

The purpose of this chapter was to introduce each part individually along with its background, considerations, and constraints. Once all of these petrophysical techniques were applied, the resulting stiffness tensors, each modeling the Woodford Shale with a different crack density, were used to calculate AVAZ results as a function of varying crack density. These results are discussed in the next chapter.

Chapter VII: AVAZ Results for Modeled Data

INTRODUCTION

AVAZ analysis was applied to field seismic data in Chapter V and showed a relative fracture intensity that is considered from "low" to "high." However, from AVAZ analysis alone, no quantitative or explicit fracture density information was obtained. Chapter VI introduced a rock physics model to evaluate the Woodford Shale at different numeric fracture densities allowing AVAZ analysis to be performed and relate the intensity (from the axes ratio) to an actual crack density. In this chapter, the resulting rock physics model was used to generate AVAZ response data for different crack densities, and an ellipse was fit to this data (method discussed in Chapter IV). From this analysis of synthetic (modeled) data, I attempt to quantify a relationship and map a crack density from the field seismic data.

ATTEMPT AT SYNTHETIC SEISMIC DATA

From the full stiffness tensor C_{ij} generated by the rock physics model (Chapter VI), synthetic seismic data were created using the ANIVEC (Mallick and Frazier, 1988) software package. However, the generation of these synthetic seismic data was deemed intractable and introduced too many unknowns into controlling the connection between crack density and the AVAZ response. Most importantly, the adjustment of model parameters and the generation of synthetic data were time-constrained and the analytic analysis performed further in this chapter was considered a better alternative, considering its flexibility and its repeatability in a timely fashion.

ANALYTIC SOLUTIONS TO AVAZ

Rüger (2001) showed that the approximation to the reflection coefficient as a function of incidence angle θ and azimuthal angle ϕ for a P-wave between two HTI media is:

$$R_P^{HTI}(\theta,\phi) = \frac{\frac{1}{2}\Delta Z}{\bar{Z}} + \frac{1}{2}\left\{\frac{\Delta\alpha}{\bar{\alpha}} - \frac{\left(\frac{2\bar{\beta}}{\bar{\alpha}}\right)^2 \Delta\mu}{\bar{\mu}} + \left[\Delta\delta^{(v)} + 2\left(\frac{2\bar{\beta}}{\bar{\alpha}}\right)^2 \Delta\gamma\right]\cos^2\phi\right\}\sin^2\theta + \frac{1}{2}\left\{\frac{\Delta\alpha}{\bar{\alpha}} + \Delta\epsilon^{(v)}\cos^4\phi + \Delta\delta^{(v)}\sin^2\phi\cos^2\phi\right\}\sin^2\theta\tan^2\theta \tag{7.1}$$

In Equation 7.1, Z is the impedance of a layer (ρV_p), α is the P-wave velocity, β is the S-wave velocity, μ is the shear modulus, and γ, $\epsilon^{(v)}$, and $\delta^{(v)}$ (Equations 2.11a, 2.14a and 2.14c, respectively) are Thomsen's anisotropic parameters.

From this equation (7.1), reflection coefficients were calculated for each azimuth as a function of incidence angle θ, and an AVO gradient B for each azimuth was interpreted from its fit to a line of the form $A + B\sin^2\theta$. Therefore, this equation allows for the fitting of an ellipse to B as a function of azimuth, similar to the AVAZ analysis performed on field seismic data in Chapter V.

Another approximation from Rüger's work allows the calculation of the AVO gradient term directly:

$$B^{iso} = \frac{1}{2}\left[\frac{\Delta\alpha}{\bar{\alpha}} - \frac{\left(\frac{2\bar{\beta}}{\bar{\alpha}}\right)^2 \Delta\mu}{\bar{\mu}}\right] \tag{7.2a}$$

$$B^{ani} = \frac{1}{2}\left[\frac{\Delta\alpha}{\bar{\alpha}} - \frac{\left(\frac{2\bar{\beta}}{\bar{\alpha}}\right)^2 \Delta\mu}{\bar{\mu}}\right] + \frac{1}{2}\left[\Delta\delta^{(v)} + 2\left(\frac{2\bar{\beta}}{\bar{\alpha}}\right)^2 \Delta\gamma\right] \tag{7.2b}$$

In these equations (7.2a-b), B^{iso} is the AVO gradient in the vertically isotropic plane of an HTI medium and B^{ani} is the AVO gradient normal to this plane. The smallest value of B would be in the direction of the isotropic plane, B^{iso} and the largest value in the direction normal, B^{ani}. Therefore, a ratio between the two would be similar to the ellipse axis ratio from AVAZ analysis. For the case of an isotropic overlaying layer (Thomsen anisotropic parameters = 0), the ratio simplifies to:

$$\frac{B^{ani}}{B^{iso}} = 1 + \frac{2\left[\frac{1}{2}\delta_2^{(v)} + \left(\frac{2\bar{\beta}}{\bar{\alpha}}\right)^2 \gamma_2\right]}{\left[\frac{\Delta\alpha}{\bar{\alpha}} - \frac{\left(\frac{2\bar{\beta}}{\bar{\alpha}}\right)^2 \Delta\mu}{\bar{\mu}}\right]} \tag{7.3}$$

This equation allows for the mapping of an ellipse axes ratio to a specific crack density, as all the terms necessary for its solving come from the C_{ij} stiffness tensor (see Chapter II), which has a crack density ε at its basis.

RESULTS

With a set of stiffness tensors C_{ij}, each calculated for a different crack density ε that was part of the Hudson (1980) cracked media model, the axes ratio was calculated from Equation 7.3. For a range of crack densities 0.01-0.09, the results are shown in Figure 7.1. Orientation does not factor into this calculation and was set *a priori.* As

expected, as the crack density increases, the ellipse was more elongated and the ratio increases. With a minimal crack density of 1%, the ellipse more represents a circle, which follows predictions that a medium with no cracks shows an AVO gradient independent of azimuth. The dependence of axis ratio on crack density is not linear, and the ratio increases more quickly for higher crack densities. From the initial relationship established here, the relative fracture intensity from AVAZ analysis of Chapter V can now be mapped to a numeric fracture density.

MAPPING CRACK DENSITIES TO SEISMIC DATA AVAZ RESULTS

From the Hudson (1980) crack model, a limitation of crack density less than 10% is imposed. As seen in Figure 7.1, the results for crack densities within this constraint show an ellipse axis ratio less than about 3. However, the field seismic data generated ellipses with axis ratios ranging from 1 to 11. Therefore, mapping the crack densities to field seismic data requires extrapolating this relationship beyond the bounds put in place by Hudson. Figure 7.2 shows the relationship between crack density and axis ratio extrapolated to 20% crack density. This higher crack density was used because pressures at Woodford depths (>13,000 ft.) allow for higher crack densities without interaction, and the Hudson (1980) model is not pressure dependent. With this range of fracture densities, the complete range of axis ratios seen in field seismic data is covered. Therefore, to fully map the AVAZ field seismic results to numeric crack densities, this extended relationship is employed. The results of this mapping are seen in Figure 7.3. The figure shows a map view of numeric crack densities and fracture orientations for the seismic survey area, similar to Figure 5.12, but with the relative fracture intensity mapped to the crack density range established after rock physics modeling.

SUMMARY

The initial relationship established here between the AVAZ ellipse ratio and the absolute crack density is non-linear (Figure 7.2). Therefore, intermediate values of the axes ratio cannot simply be scaled from one range of relative intensity to an absolute crack density without first establishing the relationship in detail. The relationship, in fact, depends on several terms for both layers in contact (Equation 7.3): the Thomsen parameters $\delta^{(v)}$ and γ, P-wave velocity α, S-wave velocity β, and shear modulus μ. These terms were carefully constrained by borehole well log data used in the rock physics modeling to represent the Woodford and the overlying Mississippian limestone. Once the connection was created, I could map a once relative term (low or high fracture intensity) to a numeric value (absolute fracture density).

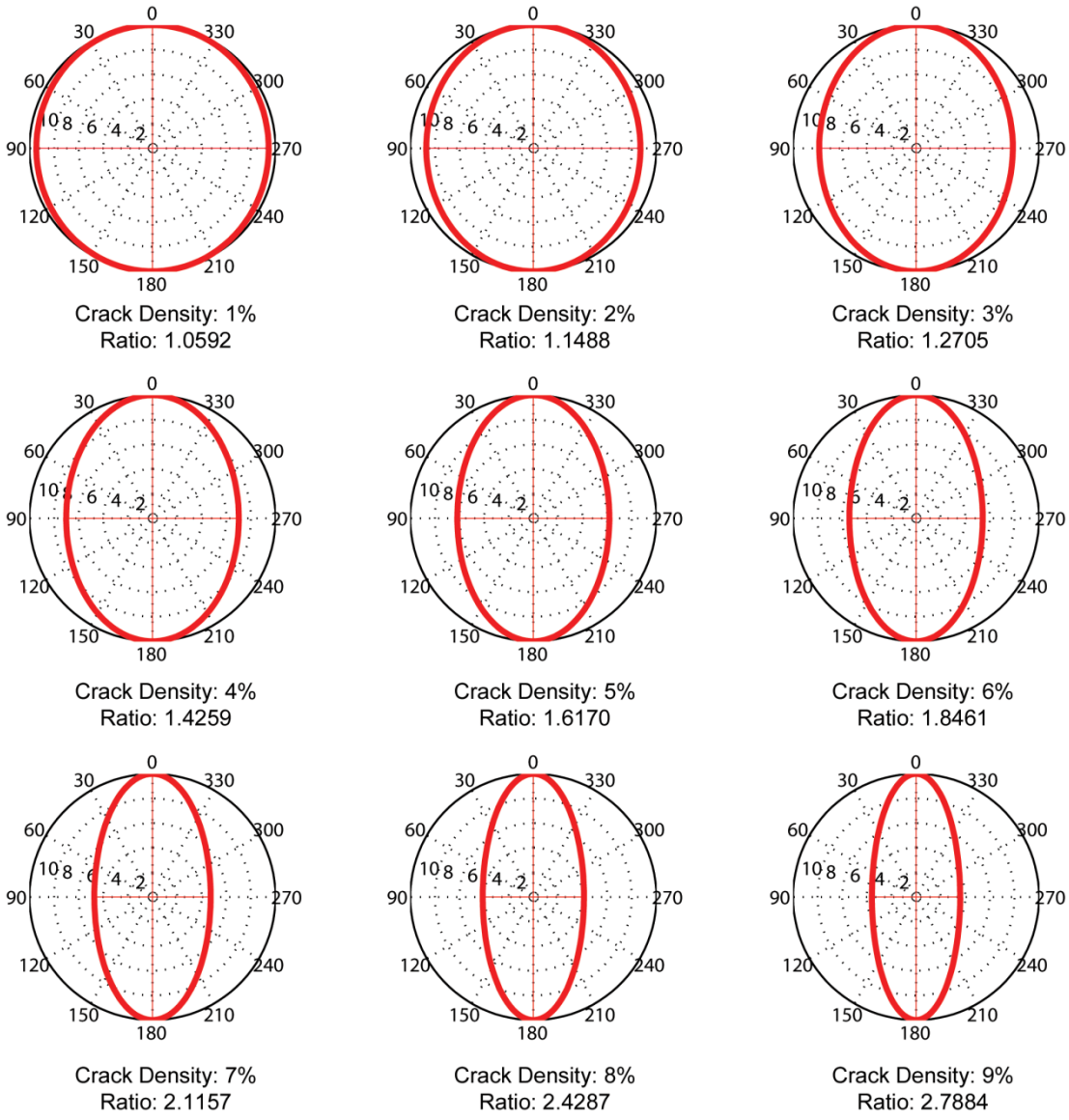

Figure 7.1 Relationship between crack density ϵ and the ellipse axis ratio (major/minor). As expected, the higher the crack density, the more elongated the ellipse. These results are calculated from a stiffness tensor C_{ij} for each crack density and Equation 7.3.

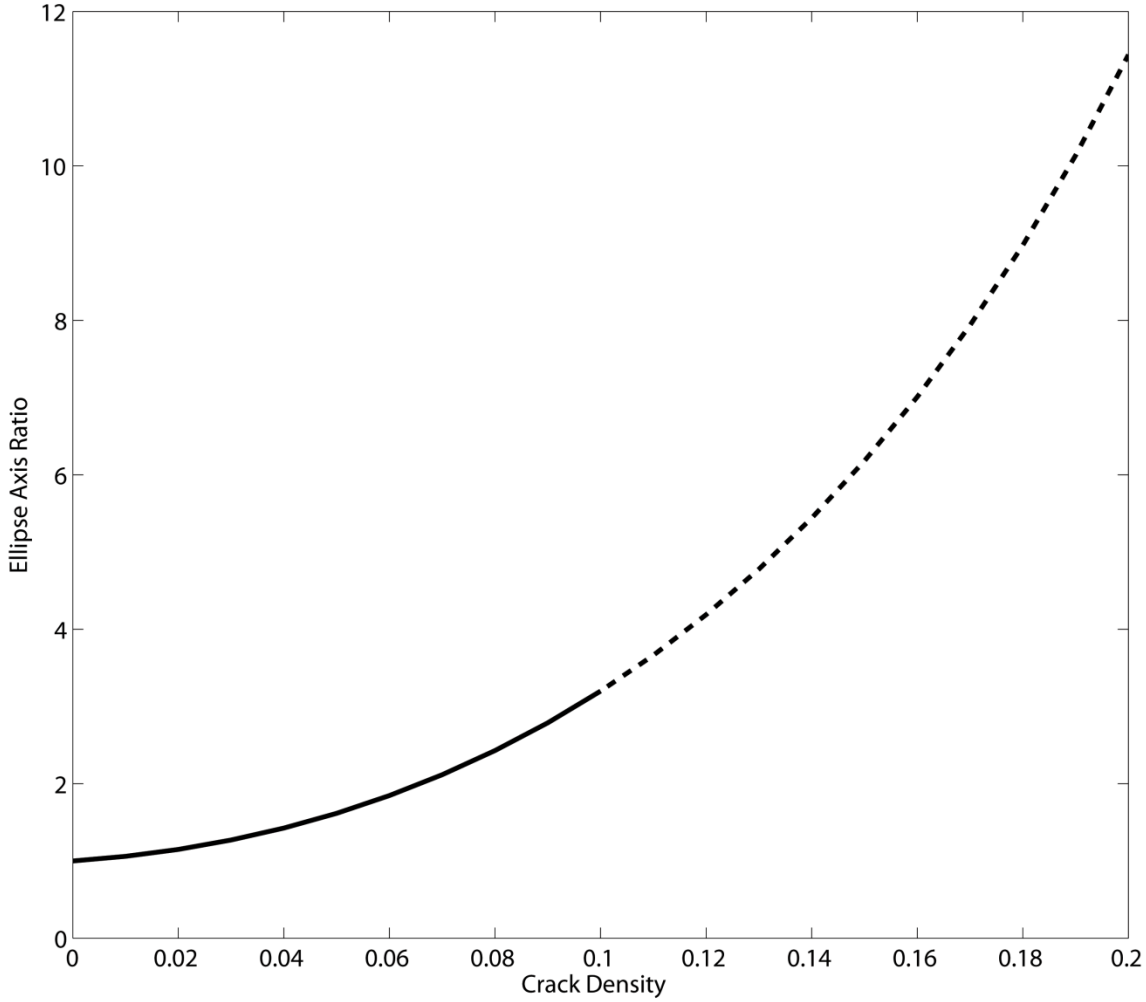

Figure 7.2 Relationship between crack density and the generated AVAZ ellipse axis ratio is shown. The Hudson (1980) cracked media model constrains crack densities to less than 10%, and values beyond this constraint are extrapolated. From this extended relationship, a mapping of field seismic data AVAZ results to numeric crack densities was performed (Figure 7.3).

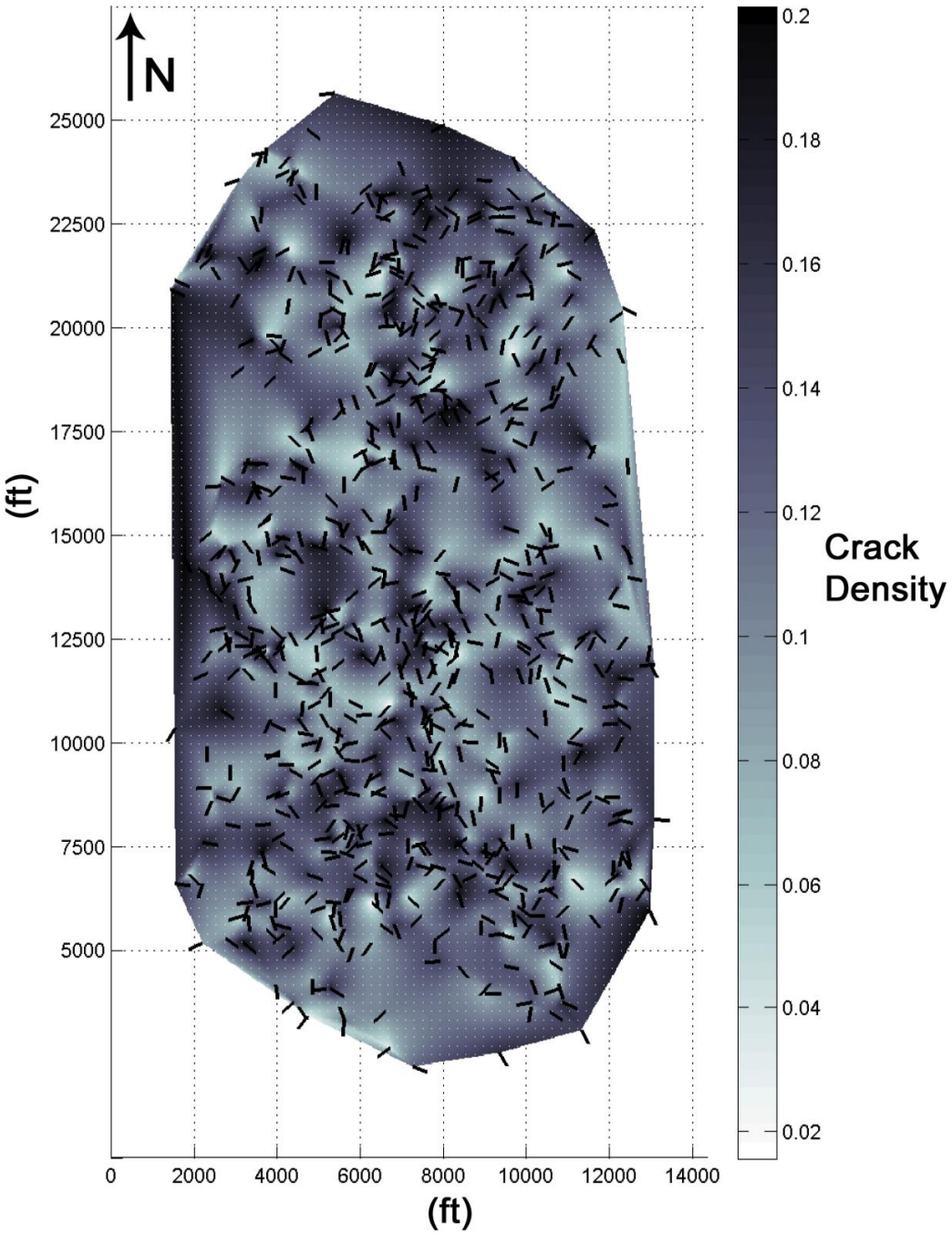

Figure 7.3 Map view of numeric crack density and fracture orientation for the seismic survey area (similar to Figure 5.12). The fracture orientation and relative crack density were calculated from AVAZ results and the mapping of relative crack density to a numeric crack density was performed using rock physics modeling.

Chapter VIII: Discussions and Conclusions

This study shows an investigation of anisotropy in the Woodford Shale in Canadian County, Oklahoma that gives potentially incongruent results using borehole logs vs. seismic data. Initially, the borehole logs show no evidence of HTI (vertical fractures) anisotropy, but did suggest the presence of vertical transverse isotropy or orthorhombic symmetry, due possibly to horizontal layering or aligned clay minerals. Sonic and, in particular, dipole sonic measurements, with their frequency well above that of seismic data, may sample too small a rock volume to give a complete description of the rock's overall anisotropic nature, especially HTI associated with large intervals between fractures. Seismic data and their significantly longer wavelengths may not be useful in detailing incremental rock properties at the scale of borehole logs, but may in fact be advantageous for volumetric properties such as fracture density and orientation. An amplitude varying with angle and azimuth (AVAZ) method was shown for calculating fracture and/or stress orientation and relative fracture density. AVAZ results, based on seismic data's longer wavelength and larger sampling scales, demonstrate azimuthal anisotropy. This is consistent with the presence of horizontal transverse isotropy due to vertical fractures or orthorhombic symmetry due to multiple fracture sets.

From AVAZ analysis of the field seismic data, a dominant fracture and/or stress orientation of WSW-ENE was resolved and a map of relative fracture intensity for the seismic survey area was generated. Fracture orientation correlated well with structural features found in the area, and establishes confidence in the methods used here. A problem with initial AVAZ analysis is the lack of an absolute crack density given from its results. To overcome this challenge, a combination of petrophysical techniques was

employed to create a rock physics model of the Woodford Shale and allowed for the generation of a relationship between numeric crack density and the axes ratio of the corresponding AVAZ ellipse. From this new relationship, AVAZ results from seismic data were then completely mapped with fracture orientation and an estimate of absolute crack density. Characterizing the fracture and/or stress orientation, a sense of spatial variation in fracture intensity, and even providing an estimate of numeric fracture density would be valuable in the search for enhanced permeability of these unconventional reservoirs and positively impact the horizontal drilling and production.

References

Aki, K. and Richards, P.G., 1980, Quantitative Seismology: Theory and Methods: W. H. Freeman and Co., San Francisco.

Andrews, R.D, 2009, Production Decline Curves and Payout Threshold of Horizontal Woodford Wells in the Arkoma Basin, Oklahoma, The Journal of the Oklahoma City Geological Society, p. 103-111.

Aoudia, K. and Miskimins, J., 2009, Analysis of rock mechanical properties by mineralogy and their potential effect from hydraulic fracturing in the Woodford shale: AAPG Search and Discovery Article #90090, 2009 AAPG Annual Convention and Exhibition.

Auld, B.A., 1973, Acoustic fields and waves in solids, Vol. 1 and 2, John Wiley & Sons, Inc., New York.

Backus, G.E, 1962, Long-wave elastic anisotropy produced by horizontal layering: Journal of Geophysical Research, Vol. 67, No. 11.

Bayuk, I., Ammerman, M., and Chesnokov, E., 2008, Upscaling of elastic properties of anisotropic sedimentary rocks: Journal Geophysics International, Vol. 172, No. 2, p. 842–860.

Berge, P.A., 1995, Constraints on elastic parameters and implications for lithology in VTI media, SEG Annual Meeting, 1995, p.1-6.

Berryman, J.G., 1979, Long wave elastic anisotropy in transversely isotropic media: Geophysics, Vol. 44, p. 896-917.

Berryman, J.G., 1995, Mixture theories for rocks. In Rock Physics and Phase Relations: a Handbook of Physical Constants, ed. T. J. Ahrens. Washington, DC: American Geophysical Union.

Boughal, K., 2008, Special focus: North America outlook unconventional resources: Geopete's View, Vol. 229, No. 8. p. 101.

Brevik, I., Ahmadi, G.R., Hatteland, T., and Rojas, M., 2007, Documentation and quantification of velocity anisotropy in shales using wireline log measurements. The Leading Edge, March 2007. p. 272-277.

Brown, R. and Korringa, J., 1975. On the dependence of the elastic properties of a porous rock on the compressibility of the pore fluid, Geophysics, Vol. 40, p. 608-616.

Burrowes, O.G. and Krause, F.F., 1987, Overview of the Devonian System: Subsurface Western Canada basin, in F. F. Krause and O. G. Burrowes, eds., Devonian lithofacies and reservoir styles in Alberta: 13th Canadian Society of Petroleum Geologists Core Conference and Display, Calgary, p. 1–20.

Caldwell, C., 2011, Lithostratigraphy of the Woodford Shale, Anadarko Basin, West-Central Oklahoma, AAPG Search and Discovery Article #50518.

Cardott, B.J., 2008, Overview of Woodford gas-shale play of Oklahoma, US: Oklahoma Geological Survey.

Castagna, J. P. and Backus M., 1993, Offset-dependent reflectivity: theory and practice of AVO analysis: Society of Exploration Geophysicists, Investigation in Geophysics, No. 8, p. 3-36.

Castagna, J.P. and Swan, H.W., 1997, Principles of AVO Crossplotting. The Leading Edge, April 1997, p. 337-342

Cheadle, S.P., Brown, R.J., and Lawton, D.C., (1991) Orthorhombic anisotropy: A physical modeling study, Geophysics, Vol. 56, p.1603-1630.

Chen, W., 1995, AVO in azimuthally anisotropic media: fracture detection using P wave data and a seismic study of naturally fractured tight gas reservoirs: Ph.D. dissertation, Stanford University.

Cluff, R.M., Reinbold, M.L., and Lineback, J.A., 1981, The New Albany Shale Group of Illinois: Illinois State Geological Survey.

Comer, J.B., 1991, Potential for producing oil and gas from Woodford Shale (Devonian-Mississippian) in the Southern Mid-continent, USA, AAPG search and discovery article #91004, AAPG annual convention meeting.

Comer, J.B., 1991, Stratigraphic analysis of the upper Devonian Woodford Formation, Permian Basin, West Texas and Southeastern New Mexico: Bureau of Economics Geology, The University of Texas at Austin, Report of investigations No. 201.

Comer, J.B., 2009, Reservoir characteristics and production potential of the Woodford Shale, with enough oil and gas to potentially become a major unconventional hydrocarbon reservoir, the Woodford is a viable play: Indiana Geological Survey, Bloomington, Indiana.

Curtis, J.B., 2002, Fractured shale-gas systems: AAPG Bulletin, Vol. 86, No. 11, p. 1921-1938.

Daley, P.F. and Hron, F., 1979, Reflection and transmission coefficient in transversely isotropic media: Geophysics, Vol.44, p. 27-38.

Ellison, S.P., 1950, Subsurface Woodford black shale, West Texas and Southeast New Mexico: Bureau of economic Geology, University of Texas at Austin Report Invest. 7, p. 21.

Fitzgibbon, A., Pilu, M., and Fisher, R.B., 1999. Direct least squares fitting of ellipses. IEEE Trans. on Pattern Analysis and Machine Intelligence, 21(5): p. 476-480.

Frantz, J.H. and Jochen, V., 2005, When your gas reservoir is unconventional, so is our solution: Schlumberger Marketing Communications.

Gray, F.D. and Head, K.J., 2000, Fracture Detection in the Manderson Field: A 3D AVAZ Case History: The Leading Edge, Vol. 19, No. 11, p. 1214-1221.

Guo, Y., Zhang, K., and Marfurt, K.J., 2010. Seismic attribute illumination of Woodford Shale faults and fractures, Arkoma Basin, OK. 80th annual SEG meeting, Expanded Abstracts, p.1372-1376.

Hall, S.A. and Kendall, J-M., 2000, Constraining the interpretation of AVOA for fracture characterization, Proceeding of the 9th IWSA, Houston, Texas, p. 107-144.

Harris, N., 2011, Mechanical Anisotropy in the Woodford Shale, Permian Basin: Origin, magnitude and scale. The Leading Edge. March 2011 p. 284-291.

Helbig, K., 1979, Discussion on the "reflection, refraction and diffraction of waves in media with elliptical velocity dependence" by F. K. Levin: Geophysics, Vol. 44, p. 987-990.

Hester, T.C., Sahl, H.L., and Schmoker, J.W., 1988, Cross sections based on gamma-ray, density, and resistivity logs showing stratigraphic units of the Woodford Shale, Anadarko Basin, Oklahoma: U.S. Geological Survey Miscellaneous Field Studies Map MF-2054.

Hester, T.C., Sahl, H.L., and Schmoker, J.W., 1990, Log-derived regional source-rock characteristics of the Woodford Shale, Anadarko Basin, Oklahoma: U.S. Geological Survey Bulletin 1866-D.

Hilterman, F.J., 1989, Is AVO the seismic signature of rock properties?, SEG Annual Meeting, 1989, p. 559-563

Hudson, J.A., 1980, Overall properties of a cracked solid: Mathematical proceedings of the Cambridge Philosophical Society, Vol. 88, p. 371–384.

Jenner, E., 2001, Azimuthal anisotropy of 3-D compressional wave seismic data, Weyburn field, Saskatchewan, Canada, Ph.D. dissertation, Colorado School of Mines, p. 197.

Jones, R.W., 1981, Some mass balance and geological constraints on migration mechanisms: AAPG Bulletin, Vol. 65, Issue 1. (January), p. 103–122.

Lambert, M.W., 1982, Vitrinite reflectance of Woodford in Anadarko basin, Oklahoma: AAPG (1982), Vol. 66, p. 591-592.

Li, X.Y., 1999, Fracture detection using azimuthal variation of P-wave moveout from orthogonal seismic survey lines: Geophysics, Vol. 64, 1193-1201.

Lynn, H.B., Simon, K.M. and Bates, C.R., 1996, Correlation between P-wave AVOA and S-wave traveltime anisotropy in a naturally fractured gas reservoir: The Leading Edge, Vol. 15, No. 8, p. 931-935.

MacBeth, C. and Lynn, H., 2001, Mapping fractures and stress using full-offset full-azimuth 3D PP data: SEG Annual Meeting, 2001., p. 110-113.

Mallick, S. and Frazer, L.N., 1988, Rapid computation of multioffset vertical seismic profile synthetic seismograms for layered media, Geophysics, Vol. 53, p. 479-491.

Mavko, G., Mukerji, T., and Dvorkin, J., 2009, The rock physics handbook: tools for seismic analysis of porous media, Cambridge University Press.

Meissner, F.F., 1978, Petroleum geology of the Bakken Formation, Williston basin, North Dakota and Montana, D. Rehrig, ed., The economic geology of the Williston basin: Proceedings of the Montana Geological Society, 24th Annual Conference, p. 207–227.

Montoya, P., 2002, Estimation of fracture orientation and relative intensity using azimuthal variation of P-ware AVO responses and oriented core data in the Tacata Field, Venezuela. SEG Expanded Abstracts 21, 261 (2002).

Mueller, M.C., 1992, Using shear waves to predict lateral variability in vertical fracture intensity: The Leading Edge, Vol. 11, No. 02, p. 29-35.

Musgrave, M.J.P., Crystal Acoustics, Holden Day, San Francisco (1970).

Northcutt, R.A. and Campbell, J.A., 1995, Geologic provinces of Oklahoma: Oklahoma Geological Survey Open-File Report 5-95, scale 1:750,000.

Ostrander, W.J., 1982, Method for interpretation of seismic records to yield indication of gaseous hydrocarbons: United States Patent No. 4,316,268.

Ostrander, W.J., 1984, Plane wave reflection coefficients for gas sands at non-normal angles of incidence: Geophysics, 49.

Pérez, M., 1996, Detection of fracture orientation using azimuthal variation of P-wave AVO responses. Geophysics, Vol. 64, p. 1253-1265.

Portas, R.M. and Slatt, R., 2010, Characterization and origin of fracture patterns in a Woodford shale quarry in Southeastern Oklahoma for application to exploration and development: AAPG search and discover article #90104, AAPG annual convention and exhibition.

Rickman, R., Mullen, M., Petre, E., Grieser, B., and Kundert, D., 2008, "A Practical Use of Shale Petrophysics for Stimulation Design Optimization: All Shale Plays Are Not Clones of the Barnett Shale," 2008 SPE Annual Technical Conference and Exhibition, 21-24 September 2008, Denver, Colorado; "SPE 115258".

Roen, J.B., 1984, Geology of the Devonian Black Shales of the Appalachian Basin, in Organic Geochemistry, Vol. 5, No. 4, p. 241-254.

Rüger, A., 1995, P wave reflection coefficients for transversely isotropic media with vertical and horizontal axis of symmetry: Expanded abstracts, Society of Exploration Geophysics, 65th annual international meeting, p. 278-281.

Rüger, A., 1996, Variation of P wave reflectivity with offset and azimuth in anisotropic media: Expanded abstracts, Society of Exploration Geophysics, 66th annual international meeting, p. 1810-1813.

Rüger, A., 2002, Reflection coefficients and azimuthal AVO analysis in anisotropic media: Society of Exploration Geophysics.

Rutherford, S.R. and Williams, R.H., 1989, Amplitude-versus-offset variations in gas sands: Geophysics, Vol. 54, N. 6, p. 680-688.

Shuey, R.T., 1985, A simplification of the Zoeppritz equations: Geophysics, Vol. 50, p. 609-614.

Sullivan, K.L., 1985, Organic facies variation of the Woodford Shale in western Oklahoma: Shale Shaker, Vol. 35, p. 76-89.

Tatham, R.H. and McCormack, M.D., 1991, Multicomponent seismology in petroleum exploration, Investigation in Geophysics Series Vol. 6, Society of Exploration Geophysicists.

Tatham, R.H., Matthews, M.D., Sekharan, K.K., Wade, C.J., and Liro, L.M., 1992, A physical model study of shear-wave splitting and fracture intensity, Geophysics, Vol. 57, No. 20, p. 647-652.

Thomsen, L., 1986, Weak elastic anisotropy: Geophysics. Vol. 51, N. 10, p. 1954-1966.

Thomsen, L., 1990, Poisson was not a geophysicist: The Leading Edge, Vol. 9, No. 12, p. 27-29.

Urban, J.B., 1960, Microfossils of the Woodford Shale (Devonian) of Oklahoma: M.S. thesis, University of Oklahoma

Vernik, L. and Nur, A., 1992, Ultrasonic velocity and anisotropy of hydrocarbon source rocks: Geophysics, Vol. 57, No. 5, p. 727–735.

Vernik, L. and Liu, X., 1997, Velocity anisotropy in shales: A petrophysical study: Geophysics, Vol. 62, No. 2, p. 521–532.

Von Almen, W.F., 1970, Palynomorphs of the Woodford Shale of south central Oklahoma with observations on their significance in zonation and paleoecology: Ph.D. dissertation, Michigan State University.

Wylie, G., 2007, Advances in fracs and fluids improve tight-gas production. Oil & Gas Journal. December 2007.

Zheng, Y., 2011, Fracture Analysis with Interpolation Before Prestack Migration. 2011 CSPG CSEG CWLS Convention.

Zoeppritz, K., 1919, Erdhebenwellen VIIIB, On the reflection and propagation of seismic waves Göttinger Nachr., I, p. 66-84.

Vita

Alexander Lamb was born in Orange County, California, USA in 1987. After attending Emerson Honors High School, he attended the University of California, Irvine where he earned two Bachelor of Science degrees in 2008, one in Physics and the other in Information and Computer Science. After two years of working in the computer science industry, he joined the M.S. program at the Jackson School of Geosciences at the University of Texas in 2010 studying exploration geophysics. He completed an internship at Devon Energy in 2011 and started work there after graduation in 2012.

Permanent email: AlexLamb@UTexas.edu

This thesis was typed by the author.